Thesis for the degree of Doctor of Philosophy

NH_3-SCR over Cu-CHA catalysts: Mechanistic insights into hydrothermal aging, water inhibition, and sulfur poisoning

Shivangi Singh

Department of Physics
Chalmers University of Technology
Göteborg, Sweden 2025

NH_3-SCR over Cu-CHA catalysts: Mechanistic insights into hydrothermal aging, water inhibition, and sulfur poisoning
Shivangi Singh
ISBN 978-91-8103-345-8

Doktorsavhandlingar vid Chalmers tekniska högskola
Ny serie nr. 5802
ISSN 0346-718X

Department of Physics
Chalmers University of Technology
SE-412 96 Göteborg
Sweden
Telephone: +46 (0)31-772 1000

Cover:
Sketch of the NH_3-SCR reaction over Cu-CHA.

Printed at Chalmers Digitaltryck
Göteborg, Sweden 2025

NH_3-SCR over Cu-CHA catalysts: Mechanistic insights into hydrothermal aging, water inhibition, and sulfur poisoning

Shivangi Singh
Department of Physics
Chalmers University of Technology

Abstract

Selective catalytic reduction using ammonia (NH_3-SCR) is a critical technology for the control of NO_x emissions from lean-burn engines. Cu-exchanged chabazite (Cu-CHA) materials are currently the preferred catalysts for NH_3-SCR thanks to their excellent activity and selectivity at low temperatures. However, Cu-CHA suffers from deactivation due to water inhibition, hydrothermal aging, and sulfur poisoning. In this thesis, detailed mechanisms for the three deactivation paths are studied by density functional theory (DFT) based kinetic modeling and reactor experiments.

At low-temperature (200 °C), high partial pressures of H_2O inhibits the NH_3-SCR by competing with NO and NH_3 for adsorption on active Cu sites. At high-temperature (>650 °C), H_2O causes hydrothermal aging, primarily through dealumination, i.e., removal of framework Al thereby Brønsted acid sites (BAS). DFT calculations reveal similar four-step hydrolysis pathways for dealumination in H-CHA and Cu-CHA, with extra-framework $Al(OH)_3(H_2O)$ formed in H-CHA and $Al(OH)_3(H_2O)$ together with Cu–Al species in Cu-CHA. The higher dealumination barriers in Cu-CHA and the thermodynamic stability of Cu–Al formation explain the experimentally observed enhanced stability of CHA in the presence of Cu. Dealumination of H-CHA is quantified by NH_3-Temperature-Programmed Desorption (NH_3-TPD) and ^{27}Al Nuclear Magnetic Resonance (^{27}Al-NMR) measurements. A quantitative comparison shows that NH_3-TPD overestimates dealumination via a self-exchange reaction in which extra-framework $Al(OH)_3(H_2O)$ accepts protons from neighboring BAS, leading to an apparent loss of acidity without framework Al removal.

Hydrothermal aging affects the kinetics of NH_3-SCR at low-temperature (200 °C). Experiments show two different deactivation mechanisms attributed to loss of BAS and decreased formation of $[Cu_2(NH_3)_4O_2]^{2+}$, which is a key intermediate for low-temperature SCR. Hydrothermal aging affects SO_2 deactivation marginally, indicating that SO_2 deactivation is largely independent of hydrothermal aging.

The proposed deactivation mechanism links loss in SCR performance to changes in Brønsted acid site and Cu speciation for each type of deactivation. The work provides mechanistic insights to improve catalyst durability during water-induced deactivation at high temperatures, high pressures and SO_2 exposure.

Keywords: NH_3-SCR, Cu-CHA, hydrothermal aging, dealumination, SO_2 poisoning, and water inhibitions.

List of Publications

This thesis is based on the following appended publications:

I. Mechanism for Cu-enhanced hydrothermal stability of Cu-CHA for NH_3-SCR
S. Singh, T.V.W. Janssens, and H. Grönbeck
Catalysis Science & Technology 14 (12), 3407-3415

II. Inhibition of NH_3-SCR over Cu-CHA at high partial pressures of water: Measurements and DFT-based kinetic modeling
S. Singh, Y. Feng, T.V.W. Janssens, and H. Grönbeck
Journal of Catalysis 446, 116071

III. Rate of NH_3-SCR over hydrothermally aged Cu-CHA
S. Singh, T.V.W. Janssens, and H. Grönbeck
Submitted

IV. Enhanced loss of Brønsted acid sites upon hydrothermal dealumination of chabazite zeolites by self-exchange with extra-framework aluminum
S. Radhakrishnan, S. Singh, C. V. Chandran, J. A. Martens, H. Grönbeck,
T. V. W. Janssens and E. Breynaert
In Manuscript

V. Impact of hydrothermal aging on the SO_2-induced deactivation of Cu-CHA catalyst for NH_3-SCR
S. Singh, T. V. W. Janssens and, H. Grönbeck
In Manuscript

My contributions to the publications

Paper I
I performed all the DFT calculations and kinetic simulations. I wrote the first draft of the paper, which was finalized together with my coauthors.

Paper II
I performed all the experiments and DFT calculations. I wrote the first draft of the corresponding parts in the manuscript.

Paper III
I performed all the experiments, DFT calculations and kinetic simulations. I wrote the first draft of the paper, which was finalized together with my coauthors.

Paper IV
I performed the NH_3-TPD experiments and DFT calculations. I wrote the first draft of the corresponding parts in the manuscript, which was finalized together with my coauthors.

Paper V
I performed all the experiments and wrote the first draft of the paper, which was finalized together with my coauthors.

Contents

Chapter 1

Introduction

Transportation plays a crucial role for the mobility of people and goods, serving as the foundation of modern economies and everyday life.[1] Heavy-duty trucks carry almost 75% of all land-based freight transport in the EU, and the vast majority of these vehicles still rely on diesel combustion engines.[2,3] Transportation with combustion engines is a significant source of air pollution and reason for climate change. Transportation emissions comprise not only carbon dioxide (CO_2), a greenhouse gas, but also other pollutants such as unburned hydrocarbons, carbon monoxide (CO), sulfur oxides (SO_x), and nitrogen oxides (NO_x).[4] Heavy-duty trucks are estimated to contribute nearly 40–50% of the total NO_x emissions from the transport sector.[5] NO_x emissions have harmful environmental impacts which includes acid rain, urban smog, and respiratory health issues.[6,7] To address these environmental and public health concerns, the EU has progressively tightened emission regulations through the Euro I–VI standards.[8] The latest development, Euro 7, significantly lowers the NO_x emission limit for heavy-duty vehicles from 460 mg/kWh under Euro 6 to 200 mg/kWh in laboratory tests and 260 mg/kWh under real-world driving conditions in Euro 7.[9] Moreover, Euro 7 introduces limits for N_2O emissions, a greenhouse gas that was not regulated under Euro 6. To comply with these strict emission standards, the development of advanced emission control technologies is necessary.[10]

The technology to reduce exhaust emissions from gasoline engines is the three-way catalyst (TWC), which has proven effective for engines operating with an air–fuel ratio close to stoichiometry.[11] The three-way catalyst simultaneously promote the oxidation of CO and unburned hydrocarbons to CO_2 and H_2O and the reduction of NO_x to harmless N_2 and H_2O. The typical three-way catalyst is based on precious metals such as platinum (Pt), palladium (Pd), and rhodium (Rh) supported on alumina (Al_2O_3) and uses ceria (CeO_2) or ceria-based materials as promoters thanks to their oxygen storage capacity.[12] The TWC is not suitable for controlling emissions from diesel engines as it requires stoichiometric air–fuel conditions. Diesel engines operate under lean conditions with excess O_2 and contains much higher levels of NO_x than exhaust from gasoline engines, making the three-way catalyst technology ineffective for NO_x reduction.[11,12]

The after-treatment system for diesel engines consists of a diesel oxidation catalyst (DOC), diesel particulate filter (DPF), NH_3-selective catalytic reduction (NH_3-SCR) system, and an ammonia slip catalyst (ASC). The DOC oxidizes CO and unburned hydrocarbons to CO_2 and H_2O. Following the DOC, the DPF captures and oxidizes soot particles.[13] SCR reduces NO_x emissions by using a reducing agent, commonly ammonia (NH_3), which reacts with NO_x over a catalyst to produce N_2 and H_2O.[14,15] Finally, the ASC removes any excess NH_3 to prevent slip into the atmosphere. Together, the diesel aftertreatment system provides an efficient emission-control strategy, and the SCR system, in particular, is highly effective for NO_x reduction of diesel exhaust.

1.1 Heterogeneous catalysis

Catalysis is essential in both natural and industrial settings.[16] Enzymes act as nature's catalysts, while synthetic catalysts are used to synthesize chemicals, produce fuels, and control emissions. Figure 1.1 shows a free energy diagram for a catalyzed reaction. The uncatalyzed reaction pathway (solid line) shows a single high energy barrier that should be surpassed to form the products. When a catalyst is introduced, the reaction proceeds via a different pathway (dotted line) involving several steps: adsorption of reactant molecules onto the catalyst, the chemical reaction, and desorption of the products. A catalyst accelerates a chemical reaction by lowering its activation energy without being consumed. As a result, it increases the rates of both the forward and reverse reactions equally, allowing the system to reach equilibrium more quickly.[16,17] Thus, the equilibrium constant remains unchanged as the catalyst does not affect the thermodynamics of the initial and final states of the catalyst. If a reaction is thermodynamically unfavorable, a catalyst does not change this situation. The catalyst can be divided into three categories: homogeneous catalyst, enzymatic catalyst, and heterogeneous catalyst.[18]

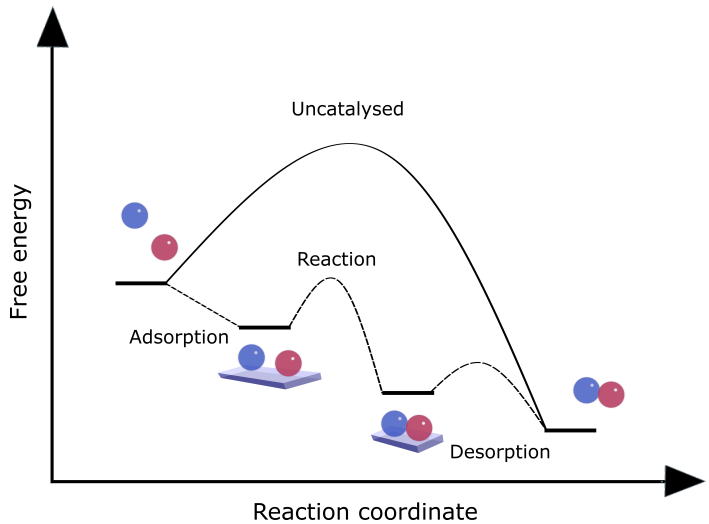

Figure 1.1: Sketch of the free energy diagram for an uncatalyzed reaction and a catalyzed reaction (dotted lines).

Homogeneous catalysts operate within the same phase as the reactants and products, typically as dissolved species in the reaction mixture, often involving coordination complexes or organometallic compounds. Enzymatic catalysts, are specialized biological molecules that accelerate biochemical reactions. In contrast, heterogeneous catalysts have a different phase from the reactants and products. An important example of a heterogeneous catalytic reaction is the Haber-Bosch process for NH_3 synthesis, where N_2 and hydrogen gases react over a metal-based catalyst to produce NH_3.[16] Other examples include the contact process for sulfuric acid production over vanadium oxide, and the use of automotive emission control catalysts like three-way catalysts and SCR in vehicles. In

this thesis, the focus is on NH_3-assisted SCR using copper-based zeolites.

1.2 NH_3 assisted selective catalytic reduction

NH_3-assisted selective catalytic reduction is a process in which NH_3 serves as a reducing agent that selectively reacts with nitrogen oxides (NO_x) in the presence of a catalyst to produce N_2 and H_2O.

In diesel engine emissions, NO_x primarily consists of nitric oxide (NO) with a smaller proportion of nitrogen dioxide (NO_2). The NH_3-SCR process can be categorized based on the predominance of NO or NO_2. The overall reaction for the, so-called, standard SCR reaction, where NH_3 reduces NO is:[19]

$$4NH_3 + 4NO + O_2 \rightarrow 4N_2 + 6H_2O \tag{1.1}$$

The NO:NH_3 stoichiometry of the reaction is one and O_2 is needed to accommodate the hydrogen atoms. Experiments with isotopically labeled reactants show that N_2 takes one nitrogen atom from NO_x and the other nitrogen atom from NH_3.[20]

When NO and NO_2 are in a 1:1 ratio, the overall reaction is given by the, so-called, fast-SCR reaction:

$$4NH_3 + 2NO + 2NO_2 \rightarrow 4N_2 + 6H_2O \tag{1.2}$$

The fast-SCR reaction does not need O_2 and is generally more facile than the standard SCR reaction. If the ratio of NO to NO_2 is below 0.5, the SCR reaction is driven primarily by NO_2 with the overall reaction:

$$8NH_3 + 6NO_2 \rightarrow 7N_2 + 12H_2O \tag{1.3}$$

This reaction has NH_3:NO stoichiometry that is higher than 1 and should therefore be avoided. Reactions (1.1) and (1.2) are preferable reaction paths for the NH_3-SCR reaction. However, there is the possibility of unselective reactions, such as the oxidation of NH_3 which produces NO_x instead of reducing it or formation of N_2O which is a potent greenhouse gas. Competing reactions are:[21]

$$4NH_3 + 3O_2 \rightarrow 2N_2 + 6H_2O \tag{1.4}$$

$$4NH_3 + 5O_2 \rightarrow 4NO + 6H_2O \tag{1.5}$$

$$2NH_3 + 2O_2 \rightarrow N_2O + 3H_2O \tag{1.6}$$

$$2NH_3 + 2NO_2 \rightarrow N_2O + N_2 + 3H_2O \tag{1.7}$$

$$6NH_3 + 8NO_2 \rightarrow 7N_2O + 9H_2O \tag{1.8}$$

1.3 Catalysts for NH_3-SCR

An ideal catalyst for selective catalytic reduction in diesel exhaust is one that exhibits following properties:

1. NO_x conversion and temperature window: The catalyst should have high activity in the temperature window of 150 °C to 550 °C. This range covers the typical dynamic exhaust temperatures during mobile operation, ensuring effective NO_x reduction from cold-start conditions around 150 °C and during highway driving or acceleration when temperatures can reach up to 550 °C.[22,23]

2. Selectivity toward N_2: The SCR catalyst must exhibit low selectivity toward N_2O (equation 1.6 to 1.8). Minimizing N_2O formation is essential both for meeting emissions regulations and for ensuring that NO_x is efficiently converted to N_2.

3. Suppression of NH_3 oxidation: Oxidation of NH_3 should be minimized (Equations 1.4–1.6) to ensure that NO_x is efficiently converted to N_2.

4. Hydrothermal stability: During Diesel Particulate Filter (DPF) regeneration, exhaust temperatures can reach up to 600–650 °C or higher to burn off accumulated soot in the DPF.[13] At these elevated temperatures, the presence of H_2O vapor can accelerate catalyst degradation, a process known as hydrothermal aging. Therefore, the catalyst must exhibit high hydrothermal stability to maintain its performance under and after these harsh regeneration conditions.[24,25]

5. Sulfur tolerance: Upon combustion of sulfur-containing compounds in diesel fuel, sulfur oxides such as SO_2 and SO_3 are formed. Exposure of the catalyst to SO_2 or SO_3 lead to significant loss of catalytic activity. Therefore, the catalyst should have resistance to sulfur.[26,27]

A variety of catalysts have been used over the years for the NH_3-SCR reaction, including noble metals,[28] transition metal oxides,[29,30] and zeolites.[31,32]

1.3.1 Noble metals

Early studies demonstrated that supported noble metals such as Pt, Pd, Rh, and Ru can catalyze the reduction of NO with NH_3. These catalysts exhibit high NO conversion below 250 °C. However, these catalyst have a low N_2 selectivity at higher temperatures due to facile NH_3 oxidation under O_2 rich conditions.[33] The high cost and limited N_2 selectivity have restricted the application of these catalyst. Nevertheless, noble metal catalysts, particularly Pt-based catalyst, are employed as ammonia slip catalysts because of their ability to selectively oxidize NH_3 to N_2 and H_2O.[34,35]

1.3.2 Transition metal oxides

The most commonly employed transition metal oxides, include vanadium (V), manganese (Mn), and iron (Fe) based systems, that have been extensively studied as NH_3-SCR catalysts.

Vanadium-based catalysts, specifically V_2O_5 supported on TiO_2 with WO_3 or MoO_3 as a promoter, are among the most commonly used catalysts for NH_3-SCR thanks to their high NO_x removal activity, good resistance to sulfur, and relatively low material cost.[36,37] Vanadia (V_2O_5) serves as an active site for NO_x removal[38], while anatase TiO_2 is regarded as the most suitable support thanks to its ability to achieve high dispersion of VO_x surface species, with WO_3 acting as a promoter for the reaction.[23] Vanadia SCR catalysts exhibit an optimal NO_x conversion in a narrow temperature window between approximately 300 °C and 400 °C.[39] Thus, vanadium-based catalysts are not suitable for mobile application, as the exhaust gas temperature are dynamic and can vary from 150 °C to 650 °C. At temperatures below 250 °C, vanadia-based catalysts exhibit poor NO_x conversion efficiency. Undesirable side reactions, such as the formation of ammonium sulfate or bisulfate, can form at low temperatures, leading to the blockage of active sites[40]. At temperatures above 500 °C, the SCR efficiency declines due to a lack of thermal stability, primarily attributed to deactivation of TiO_2 anatase to inactive TiO_2 rutile accompanied by a loss of surface area and sintering of the VO_x.[23] Other important challenges are the unwanted formation of the N_2O at high temperatures and generation of toxic volatile vanadia species, which can cause hazard risks to human health and the environment.[23,36,41] Therefore, V_2O_5-based catalysts are better suited for stationary applications, where the operating temperature can be controlled.

Other transition metal oxides like Mn-based oxides are also promising catalyst for NH_3-SCR. MnO_2/TiO_2 exhibits exceptional low-temperature activity, however, N_2 selectivity is low and so is the resistance to SO_2 poisoning.[42] Therefore, bimetallic system such as Mn-Ce bimetallic systems were developed, which improved the N_2 selectivity at low temperatures[43,44]. However, Mn-Ce based catalyst suffers from low N_2 selectivity at higher temperatures and deactivation when exposed to SO_2.[42,43,45]

1.3.3 Metal-exchanged zeolite catalysts

Zeolites are alumino-silicates, with tetrahedral units of SiO_4 and AlO_4.[46] The tetrahedral units form rings of different size, which make up the porous zeolite structure. The substitution of Si by Al in the structure introduces an effective negative charge, which is balanced by protons, creating Brønsted acid sites.[47] Brønsted acid sites plays a crucial role in zeolites catalytic properties. The protons can be exchanged with metal cations like Na, K, Fe, and Cu. Such metal-exchanged zeolites exhibit Lewis acidity, enhancing their catalytic performance in various reactions.[48,49]

The most relevant zeolite frameworks for NH_3-SCR are Beta (BEA), ZSM-5 (MFI), and CHA (SSZ-13). Beta, ZSM-5, and CHA zeolites are characterized by their pore sizes and ring structures, which influence the catalytic performance. Beta is a large-pore zeolite with 12-membered ring windows (∼7.6 Å), and ZSM-5 is a medium-pore zeolite with 10-membered ring windows (∼5.5–5.6 Å). CHA, or Chabazite, as shown in Figure 1.2 is a small-pore zeolite with 8 oxygen atoms in their largest pore windows with pore opening of approximately 3.8 Å, In addition to the eight membered ring, the structure contains along with four and six membered ring.[50]

Among metal-exchanged zeolites, Cu and Fe-exchanged zeolites have demonstrated outstanding performance in NH_3-SCR applications.[49] They offer a broad operational

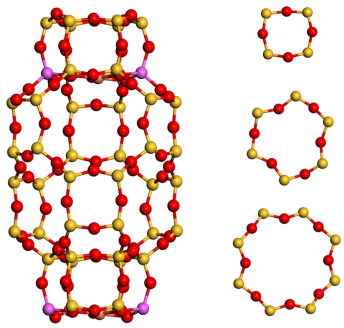

Figure 1.2: Ball and stick model of the CHA structure with 4, 6, and 8 membered ring. Atomic color code: aluminum (purple), silicon (yellow), and oxygen (red).

temperature range compared to V_2O_5-based catalysts and good resistance to sulfur poisoning.[50] Although Fe-zeolites such as Fe-BEA exhibit superior high-temperature NO_x reduction activity (above 400 °C) compared to Fe-ZSM-5 and Fe-CHA, their practical application remains limited because Fe-based zeolite catalysts generally suffer from poor hydrothermal stability, which leads to rapid dealumination and $FeAlO_x$ aggregation.[51,52] [15]

Larger-pore Cu-ZSM-5 and Cu-BEA catalysts exhibit good activity for NH_3-SCR, but they are more susceptible to hydrocarbon poisoning, which limits their application under real exhaust conditions. Cu-CHA demonstrates superior performance over Cu-ZSM-5 and Cu-BEA catalysts. Cu-CHA has excellent low-temperature activity and good hydrothermal stability primarily thanks to its small-pore geometry.[51,53,54] Additionally, Cu-CHA tends to produce less nitrous oxide (N_2O) compared to other zeolites like BEA and ZSM-5.[54] Thus, Cu-CHA is the preferred and commercially implemented catalyst for NH_3-SCR.

NH_3-SCR reaction is a redox reaction that proceeds via alternating reduction and oxidation steps where Cu changes oxidation state between Cu^I and Cu^{II}. O_2 adsorbs on Cu^I sites forming Cu^{II}, whereas the coupling between NO and NH_3 reduces Cu^{II} to Cu^I.[55,56]The Cu-ions are solvated by NH_3 at temperatures below 300 °C and the reaction proceeds over mobile $[Cu(NH_3)_2]^+$ complexes[57–60]. The mobility of the complexes is critical as it facilitates the formation of pairs of complexes that are required to activate O_2[61–63]. O_2 adsorption results in a $[Cu_2(NH_3)_4O_2]^{2+}$ peroxo species, which is a key intermediate as it enables NO adsorption. In subsequent steps, it has been proposed that adsorbed NO reacts with NH_3 forming H_2NNO and HONO. The H_2NNO and HONO intermediates decompose thereafter with low barriers to N_2 and H_2O over Brønsted acid sites[56,64].

1.4 Objective

The objective of this thesis is to explore the deactivation mechanisms of the Cu-CHA catalyst caused by water inhibition, hydrothermal aging, and sulfur poisoning under

various temperatures and pressures. To address these issues, Density Functional Theory (DFT) calculations and microkinetic modeling are combined with experimental studies. This combined approach enables to relate deactivation pathways to changes in active sites and their impact on the SCR reaction rate. The overall aim is to gain a deeper understanding of the materials properties of Cu-CHA to improve its durability and stability in NH_3-SCR applications.

The influence of high H_2O partial pressures on low-temperature (200 °C) NH_3-SCR over Cu-CHA catalysts is studied by identifying the competitive adsorption behavior of H_2O relative to NH_3 and NO on the active Cu sites. The effect of H_2O at high-temperatures (650 °C) is also investigated, focusing on dealumination as one of the primary mechanisms for decreased hydrothermal stability of CHA. The role of Cu in enhancing the hydrothermal stability of the CHA framework is explained through a DFT proposed mechanism of dealumination in H-CHA and Cu-CHA. Further, dealumination in H-CHA is quantified using NH_3-TPD and ^{27}Al-NMR and a self-exchanged reaction is proposed in dealuminated H-CHA.

The NH_3-SCR mechanism over hydrothermally aged catalysts is explored. Two distinct deactivation processes are identified: an initial rapid deactivation linked to loss of the Brønsted acid sites, followed by a slower deactivation related to Cu sites. Finally, the effect of hydrothermal aging prior to SO_2 exposure is assessed to understand its influence on the extent of SO_2-induced deactivation and the regeneration of the Cu-CHA across different aging temperatures and durations.

This thesis, which in parts is based on my licentiate thesis,[65] contains six chapters. Chapter 1 provides an introduction to the research topic. Chapter 2 discusses the electronic energies obtained from density functional theory (DFT), while Chapter 3 focuses on the materials properties derived from DFT calculations. Chapter 4 outlines the experimental procedures employed, Chapter 5 discusses deactivation pathway of Cu-CHA and Chapter 6 presents the conclusions and outlook.

Chapter 2

Electronic structure calculations

Electronic structure calculations play a crucial role in understanding materials properties at a fundamental level. In catalysis, electronic structure calculations are used to explore bond strengths, structures, and reaction mechanisms. The electronic structure is obtained by solving the Schrödinger equation, which has long posed challenges in terms of finding solutions. To address this issue, there has been a progression from Hartree-Fock approximations to the Density Functional Theory (DFT). This chapter focuses on electronic structure calculations, with an emphasis on the Density Functional Theory (DFT).

2.1 The Schrödinger equation

The time-independent, non-relativistic Schrödinger equation is given by [66]:

$$\hat{H}\Psi = E\Psi \tag{2.1}$$

where $\hat{H}$, Ψ and E are the Hamiltonian energy operator, wave function, and the total energy of the system, respectively. The total wavefunction Ψ contains all the information and properties of the system and is fundamental in a quantum mechanical description. However, the real physical interpretation of Ψ lies when it is squared ($|\Psi|^2$), which can be interpreted as the probability density of the particle described by the wave function Ψ.

The Schrödinger equation is complex and solvable only for hydrogen-like systems. The Born-Oppenheimer approximation is generally the first approximation when solving the Schrödinger equation. [67] The nuclei, being much more massive than the electron (1840 times in case of hydrogen), lead electrons to quickly occupy the ground state configuration whenever a nucleus moves. This assumption allows us to consider the position of nuclei as fixed and consider the total wavefunction as the product of the wavefunction for the electrons and the wavefunction for the nucleus.

The Hamiltonian operator $\hat{H}$ in equation 2.1, is a sum of the kinetic and potential operators involved.

$$\hat{H} = E_I^{\text{kin}} + E_i^{\text{kin}} + U_{Ii} + U_{ij} + U_{IJ} \tag{2.2}$$

where, E_I^{kin} and E_i^{kin} are the kinetic energy operators of the nuclei and electrons, respectively. U_{Ii}, U_{ij}, U_{IJ} are the potential energy operators describing the Coulomb interactions between nucleus–electron, electron-electron, and nucleus–nucleus, respectively. As a result of the Born-Oppenheimer approximation, the Hamiltonian for the electrons is described as:

$$\hat{H}_e = E_i^{\text{kin}} + U_{Ii} + U_{ij} \tag{2.3}$$

2.2 Early first-principles calculations

The Schrödinger equation is solvable only for single-electron systems. To tackle many-body problems, approximations are employed. Hartree's approach simplifies this by treating each electron independently, representing interactions with others via an average electron density instead of individual interactions.[68] This transforms the complex n-electron system into a set of non-interacting one-electron systems influenced by an average field.

$$\left(-\frac{1}{2}\nabla_i^2 + U_{\text{ext}}(\mathbf{r}) + U_H(\mathbf{r})\right)\psi_i(\mathbf{r}) = E\psi_i(\mathbf{r}) \tag{2.4}$$

where, U_{ext} is the attractive interaction between electrons and nuclei, U_H is the Hartree potential coming from the classical Coulomb repulsive interaction between each electron and the mean field of all electrons. Here, the Hamiltonian is expressed in atomic units (a.u.), which form a system of natural units that is particularly convenient for atomic-scale calculations.[i] The N-electron wave function can be simply approximated as the product of N numbers of one-electron wave functions:

$$\Psi_e = \psi_1 \times \psi_2 \times \cdots \times \psi_n \tag{2.5}$$

In the Hartree-Fock method,[69] the N-electron wavefunction is approximated as a linear combination of non-interacting one-electron wave functions arranged in the form of a Slater determinant. This wavefunction follows the antisymmetry principle, ensuring that the wave function changes sign when the coordinates of any two electrons are exchanged, reflecting the fermionic nature of electrons, which was neglected in the Hartree method. The Hartree-Fock approach seeks to find the set of wave functions that minimizes the total energy of the system by iteratively solving the Schrödinger equation. However, the Hartree-Fock method fails to accurately describe systems with pronounced electron correlation, which leads to inaccuracies in describing the chemical bonds.[70]

2.3 The density functional theory

The concept of working with electron density rather than wavefunctions originated in 1927 when Thomas and Fermi independently introduced the idea.[71,72] However, the formal verification awaited Hohenberg and Kohn's two theorems in 1964.[73] The first theorem asserts that a unique external potential U_{ext} is solely determined by the ground-state electron density, implying that the energy can be expressed as a functional of the electron density. As the external potential determines the system's Hamiltonian, and the Hamiltonian dictates all properties of the system, it follows that the ground-state electron density effectively governs all ground state properties of the system, including the ground-state wavefunction.[74]

The second theorem by Hohenberg and Kohn proves that the ground state of a system can be determined using the variational principle. The electron density giving the lowest

[i]Atomic units (a.u.) constitute a system of natural units that is convenient for atomistic calculations. In this system, the electron mass m_e, the elementary charge e, the reduced Planck constant $\hbar$, and the Coulomb force constant $4\pi\varepsilon_0$ are all set to unity.

energy value represents the true ground-state electron density, which can subsequently be utilized to compute various system properties.[74]

Later, Kohn and Sham proposed an approach to evaluate the density functional.[75] In the Kohn-Sham approach, electrons are assumed to be non-interacting, following the mapping of the interacting N-electron system onto a non-interacting one-electron system under the given external potential. This fictitious system of non-interacting electrons effectively captures the essential electronic structure of the original many-body system.[75] The energy functional in the Kohn-Sham approach is defined by:

$$E_{\mathrm{KS}} = T_0[n(\mathbf{r})] + \int n(\mathbf{r}) V_{\mathrm{ext}}(\mathbf{r})\, d\mathbf{r} + E_H[n(\mathbf{r})] + E_{xc}[n(\mathbf{r})]. \tag{2.6}$$

Here, n($\mathbf{r}$) is the electron density, the first term is the kinetic energy of the non-interacting electrons, and the second term is the interaction between the electrons and the external potential. The third term (Hartree energy) is the classical electron-electron interaction. The last term is the exchange-correlation energy, which also includes the kinetic energy resulting from the interactions between the electrons. This will be discussed in next section. By applying the variational principle on the Kohn-Sham energy functional

$$\frac{\delta E_{\mathrm{KS}}}{\delta \psi_i^*(\mathbf{r})} = 0, \tag{2.7}$$

it is possible to derive the Kohn-Sham equation for an electron i with the single electron wavefunction ψ_i

$$-\frac{1}{2}\nabla^2 \psi_i(\mathbf{r}) + \left[V_{\mathrm{ext}}(\mathbf{r}) + \int \frac{n(\mathbf{r}')}{|\mathbf{r} - \mathbf{r}'|}\, d\mathbf{r}' + \frac{\delta E_{xc}}{\delta n(\mathbf{r})} \right] \psi_i(\mathbf{r}) = \epsilon_i \psi_i(\mathbf{r}). \tag{2.8}$$

This reformulation and treatment of independent electrons provides a much easier and more effective way of calculation. Over the years, it has been demonstrated that this approach closely mimics the true ground-state density, enabling the description of chemical bonds with reasonable accuracy.[76]

2.3.1 Approximations to the exchange-correlation functional

The exchange-correlation part of the energy functional plays a crucial role as it should capture many-body quantum mechanical effects.[77] The exchange energy term originates from the quantum mechanical exchange interaction, reflecting the antisymmetry of the electron wavefunction. This term quantifies the energy associated with the exchange of electrons with the same spin, meaning that two electrons cannot occupy the same quantum state. The correlation energy term accounts for the correlated motion of electrons.[76]

Local density approximation

The Local Density Approximation (LDA) is a simple estimation of the exchange-correlation (xc) energy in many-electron systems. It assumes a locally uniform electron density, allowing the calculation of the exchange-correlation energy based on the properties of a homogeneous electron gas. This approach treats complex systems as composed of small,

uniform pieces with constant electron density.[75] The exchange and correlation energies per electron in a homogeneous electron gas can be accurately calculated using quantum Monte Carlo simulations and can be represented analytically[78]:

$$E_{xc}^{\mathrm{LDA}}[n(\mathbf{r})] = \int \epsilon_{xc}^{\mathrm{hom}}[n(\mathbf{r})]n(\mathbf{r})\, d\mathbf{r}, \tag{2.9}$$

LDA is effective for calculating the lattice parameters for various materials, particularly those with slowly changing electron density. Nevertheless, LDA tends to over-estimate the cohesive energies, by as much as 1 to 2 eV, and falls short in representing systems with rapidly varying electron density and strong correlations.

Generalized gradient approximation

The Generalized Gradient Approximation (GGA) represents an improvement over the Local Density Approximation (LDA). GGA incorporates both local and semi-local information by considering the electron density and its gradient at a specific point .[79,80] The general form of GGA in practice is expressed based on the LDA with an additional enhancement factor F(s) that directly modifies the LDA energy:

$$E_{xc}^{GGA}[\mathbf{r}, s] = \int \epsilon_{xc}^{LDA}[n(\mathbf{r})]n(\mathbf{r})F(s)\, d\mathbf{r} \tag{2.10}$$

$$s = C\frac{|\nabla n(\mathbf{r})|}{n^{4/3}(\mathbf{r})} \tag{2.11}$$

Here, s is defined as a dimensionless quantity that depends on the electron density $n(\mathbf{r})$ and its gradient $\nabla n(\mathbf{r})$, scaled by a constant C. GGA addresses some of LDA's limitations by considering the inhomogeneities in electron density distribution. This leads to more accurate predictions of structural properties, reaction energies, and molecular geometries, particularly in systems with rapidly changing electron densities. One of the GGA functional is the Perdew, Burke, and Ernzerhof (PBE) functional, which is used in this thesis.[79] This functional is widely employed in DFT calculations because it has errors typically within the range of 0.5 eV.[81,82]

Hybrid GGA

One of the main reasons for the inaccuracy in GGA is electron self-interaction. The self-interaction error arises from the method used to compute Hartree energy using the total electron density. In the Kohn-Sham DFT approach, each electron is considered to move within an effective potential generated by all electrons, including itself. This formulation results in each electron erroneously interacting with its own charge distribution when solving the Kohn-Sham equations, thus, introducing a self-interaction error. To reduce this self-interaction error, hybrid functionals can be used. As the name suggests these are GGA-type functionals combined with some $\sim 25\%$ of the Fock exchange energy from the Hartee-Fock method.[83] The Fock exchange component does not suffer from self-interaction error, thus, improving the description of electron localization, charge transfer, and band gaps.

DFT+U

DFT+U is a simple computational method that addresses the self-interaction error in LDA and GGA functionals. The approach is generally used for materials with partially filled d or f orbitals, such as transition metals and rare-earth elements.[84] In DFT+U, the "U" represents the Hubbard U parameter, a correction term that considers the on-site Coulomb interaction among electrons within the same atomic orbital. This corrects the self-interaction errors of DFT and improves the treatment of localized electrons.[85,86] DFT+U is less computationally intensive than hybrid functionals, which require the calculation of exact exchange from the Hartree-Fock theory. In this thesis, DFT+U method is used to describe the localized Cu(3d) electrons.

van der Waals interaction

The local (LDA) and semi-local (GGA) exchange-correlation functionals do not include van der Waals interactions, which arise due to long-range interaction of instantaneous dipoles. One of the approaches to effectively describe the vdW interactions is DFT-D3 developed by Grimme and co-workers[87]. This correction adds a pairwise attractive potential decaying with the inverse sixth power of the distance between atoms, typical for van der Waals forces.[88] DFT-D3 is used in this thesis.

2.3.2 Solving the Kohn-Sham equations

Plane wave basis set

The Kohn-Sham orbitals and electron density need to be expanded. Different basis can be used e.g. Gaussians, atomic orbitals, and plane waves.[84] In this work, the Vienna Ab initio Simulation Package (VASP) code has been used[89], which is a plane wave method. Plane waves are nonlocal and span the entire space. Bloch's theorem is a fundamental principle that describes how electrons move in a periodic potential.[90] Additionally, Bloch's theorem plays a crucial role by stating that the wave functions of electrons in a solid can be represented as the product of a plane wave and a function that shares the same periodicity as the crystal lattice.

$$\psi_k(\mathbf{r}) = u_k(\mathbf{r}) \exp(i\mathbf{k} \cdot \mathbf{r}) \tag{2.12}$$

Here $u_k(\mathbf{r})$ is a periodic function that has the same periodicity as the potential such that $u_k(\mathbf{r})u_k(\mathbf{r}) = (\mathbf{r} + \mathbf{R})$.[84]

Pseudopotentials

A significant challenge in electronic structure calculations arises from the different characteristics of electronic wavefunctions in different region of space. Electrons located far from the atomic core typically have smooth wavefunctions, while electrons localized in the core exhibit high-frequency oscillations, complicating the use of plane waves for their representation. To address this issue, pseudopotentials are employed.[91] Pseudopotentials are created to mimic the true potentials of the valence electrons without the need to

account for the core electrons. This is achieved through the process of pseudization, which simplifies the wave functions of valence electrons, making them smoother. Various types of pseudopotentials exist[84], among which the projector augmented wave (PAW)[90] method is used in this thesis. The method involves mapping both core and valence wave functions separately. Valence wave functions (ψ_{inter}) are represented using plane-wave expansions, while core wave functions (ψ_{core}) are projected onto a radial grid centered at the atom. By adding these two components and trimming off the overlapping part (ψ_{net}), the final wave function (ψ_{PAW}) closely resembles the AE wave function.[76]

$$\psi_{\text{PAW}} = \psi_{\text{inter}} + \psi_{\text{core}} - \psi_{\text{net}} \tag{2.13}$$

Solving the Kohn-Sham equation

The potential experienced by the electrons depends on the charge density, see equation 2.6. Thus, to achieve self-consistency in the electronic structure calculations, a Self-Consistent Field (SCF) loop is necessary.[76] Initially, the electron densities from each atom in its isolated state are superimposed to construct the starting electron density. Then, E_{xc} and other relevant terms are computed to determine the Kohn-Sham (KS) Hamiltonian. Following this, the set of coupled KS equations is solved to derive the KS orbitals. Using these orbitals, a new electron density is calculated, which includes a mix of the previous densities to refine the approximation. This iterative process continues until the change in energy or density is less than a specified threshold, usually 10^{-4} to 10^{-5} eV, indicating that self-consistency has been reached. At this point, the ground-state energy has been evaluated for the given the nuclear coordinates.

Chapter 3

Calculations of materials properties

In this chapter, we discuss how computational methodologies can be employed to derive materials properties from electronic structure calculations. Specifically, we explore methods for optimizing structures, calculating reaction barriers, and vibrational frequencies. Additionally, we will discuss how kinetic model can be constructed and analyzed.

3.1 Geometry optimization

The most relevant molecular structures are local or global energy minima. The optimization process begins with minimizing the electronic energy at a fixed ionic position. After each electronic relaxation, the force acting on each ion is calculated. The force acting on the nucleus is the gradient of the total energy with respect to atomic positions.

$$F_I = -\left(\psi \left| \frac{\partial \hat{H}}{\partial R_I} \right| \psi\right) = \int n(\mathbf{r}) \left(\frac{Z_I(\mathbf{r}-\mathbf{R}_I)}{|\mathbf{r}-\mathbf{R}_I|^3}\right) d\mathbf{r} + \sum_{J\neq I} \frac{Z_I Z_J(\mathbf{R}_I-\mathbf{R}_J)}{|\mathbf{R}_I-\mathbf{R}_J|^3}, \qquad (3.1)$$

The forces are calculated using the Hellmann–Feynman theorem,[92,93] which relates the force on a nucleus to the derivative of the expectation value of the electronic Hamiltonian with respect to its position, under the Born–Oppenheimer approximation. The integral is the electrostatic force on nucleus I due to the charge distribution of the electrons, $n(\boldsymbol{r})$. The second term represents the repulsive electrostatic force between nuclei I and J with the charges of the nuclei being Z_I and Z_J, respectively. After multiple iterations of minimizing electronic and atomic energies, the system will eventually attain its minimum-energy arrangement, characterized by forces on each atom approaching zero. There are different methods that can be implemented for minimization: the quasi-Newton method, the conjugate gradient (CG) method, and the damped MD method.[70] In this thesis, the conjugate gradient method has been used.[76] The method begins with an initial geometry, calculates the energy gradient, and uses the energy gradient to set a search direction which is initially the steepest descent. Through line searches, it adjusts atom positions, updating the search direction to be conjugate to previous directions, ensuring efficient convergence. The geometries obtained from these calculations can be compared to experimental data using, for example, diffraction techniques.[94] Sometimes, it can be difficult to locate the global minimum due a flat potential energy surface. To obtain lower energy structure in such cases, *ab initio* molecular has been used, which is discussed later in this chapter.

3.2 Finding transition states and energy barriers

Svante Arrhenius introduced a phenomenological equation in 1889, proposing a relationship to describe the temperature dependence of the rate constant for a reaction reaction.[95,96] The equation, which now is called the Arrhenius equation is:

$$k = A \exp\left(-\frac{E_a}{k_{\mathrm{B}}T}\right) \tag{3.2}$$

Here, E_a is the activation energy required for the reactants to be converted into the products. Experimentally, E_a can be determined by plotting the natural logarithm of the rate constant against the inverse temperature (T^{-1}). The slope of this plot provides -$\mathrm{E}_a/\mathrm{k}_B$. The apparent activation energy in equation 3.2 is an empirical parameter that characterizes how the rate of a reaction responds to changes in temperature. The activation energy calculated from the Arrhenius equation represents a global, overall description of the reaction. The reaction generally consists of multiple elementary steps, each associated with its own energy barrier. The elementary reaction barrier is the energy difference between the reactant and the transition state (the highest energy point along the reaction coordinate) for a single reaction step.

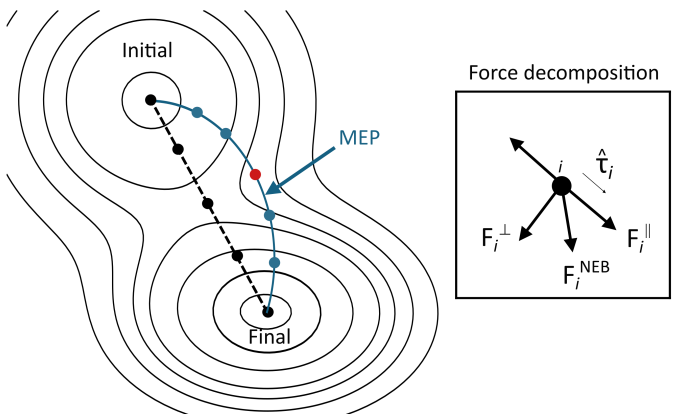

Figure 3.1: Schematic of the nudged elastic band (NEB) method. This figure is adapted from Ref.[97]

One widely used method for finding the transition state is the nudged elastic band method (NEB),[98,99] which is used in this thesis. In this method, the Minimum Energy Path (MEP) is determined by generating a series of intermediate images between the initial (reactant) and final (product) states. During optimization, only the component of the true force that is perpendicular to the path is used to relax each image, while the parallel component of the spring force is applied. In this way, the spring forces control the spacing of the images and maintain continuity of the path and, hence, the term elastic band. The total force acting on each image is, therefore, the sum of the perpendicular

true force and the parallel spring force, as illustrated in Figure 3.1, given by:[97]

$$\mathbf{F}_i = \mathbf{F}_i^{\parallel} - \nabla E(\mathbf{R}_i)_{\perp}, \tag{3.3}$$

where the true force is given by

$$\nabla E(\mathbf{R}_i)_{\perp} = \nabla E(\mathbf{R}_i) - (\nabla E(\mathbf{R}_i) \cdot \hat{\tau}_i)\,\hat{\tau}_i \tag{3.4}$$

Here, E is the energy of the system, which is a function of all the atomic coordinates, and $\hat{\tau}_i$ is the normalized local tangent at image i. The spring force is

$$\mathbf{F}_i^{\parallel} = k(|\mathbf{R}_{i+1} - \mathbf{R}_i| - |\mathbf{R}_i - \mathbf{R}_{i-1}|)\hat{\tau}_i, \tag{3.5}$$

where k is the spring constant. An optimization algorithm is used to move the images according to the force. This selective force projection "nudges" the images so that they do not fall downhill into the energy minima or cut across the potential energy surface. Sometimes, it is possible that the image is not exactly at the saddle point, and for that case, we can use the climbing image NEB (CI-NEB)[98] method in which the information about the Minimum Energy Path (MEP) is preserved, while also achieving a precise convergence to a saddle point.

3.3 Vibrational analysis

Vibrational frequencies are essential for various purposes like determining vibrational entropy, zero-point energy, identifying minima, transition states, and molecule-specific vibrations. These frequencies represent the oscillations of atoms around their equilibrium positions.

Calculating the vibrational frequencies requires expanding the total energy of the system around its equilibrium configuration within the harmonic approximation. For a system of N atoms, the Cartesian coordinates are collected into the vector $\mathbf{r} = (r_1, \ldots, r_{3N})$. If $\mathbf{r}_0$ denotes the optimized geometry, the displacements from equilibrium are defined as $\Delta\mathbf{x} = \mathbf{r} - \mathbf{r}_0$. The potential energy can then be expressed using a second-order Taylor expansion[100]:

$$E(\Delta\mathbf{x}) = E_0 + \frac{1}{2}\sum_{i=1}^{3N}\sum_{j=1}^{3N} \left.\frac{\partial^2 E}{\partial x_i \partial x_j}\right|_{\Delta\mathbf{x}=0} \Delta x_i \Delta x_j, \tag{3.6}$$

This approach, which neglects the higher-order terms in the Taylor expansion, is called the harmonic approximation.[84] The first derivative in equation 3.6 is zero because the system is at equilibrium. The second term is the second-order partial derivative of the energy E with respect to coordinates x_i and x_j evaluated at the equilibrium position x_0 and multiplied by the product of the displacements Δx_i and Δx_j. If we define

$$H_{ij} = \left[\frac{\partial^2 E}{\partial x_i \partial x_j}\right]_{\mathbf{x}=\mathbf{x}_0} \tag{3.7}$$

then these derivatives define a $3N \times 3N$ matrix known as the Hessian matrix, which describes the curvature of the potential-energy surface. The full set of normal modes can

be evaluated by using the finite-difference approximations to obtain the elements in the Hessian matrix.

$$H_{ij} \approx \frac{E(+\delta x_i, +\delta x_j) - 2E_0 + E(-\delta x_i, -\delta x_j)}{\delta x_i \, \delta x_j}. \tag{3.8}$$

Within the harmonic approximation, the nuclear motion can be written as

$$\frac{d^2\mathbf{x}}{dt^2} = -A\,\mathbf{x}, \tag{3.9}$$

where A is the mass–weighted Hessian matrix with elements

$$A_{ij} = \frac{H_{ij}}{\sqrt{m_i m_j}}. \tag{3.10}$$

The vibrational modes of the system are obtained by solving the eigenvalue equation

$$A\,\mathbf{e}_i = \lambda_i\,\mathbf{e}_i, \tag{3.11}$$

where the eigenvalues are related to the vibrational frequencies by

$$\nu_i = \frac{\sqrt{\lambda_i}}{2\pi}. \tag{3.12}$$

Having determined the normal-mode frequencies ν_i, the corresponding quantized vibrational energy levels are given by

$$E_{i,n} = h\nu_i \left(n + \frac{1}{2}\right), \qquad n = 0, 1, 2, \ldots, \tag{3.13}$$

where h is Planck's constant. The vibrational frequencies obtained from these calculations can be compared to experiments using, for example, infrared spectroscopy (IR).

3.4 Ab initio molecular dynamics

In this thesis, Molecular Dynamics is employed to explore and identify minimum energy structure of different Cu species in CHA. Molecular Dynamics (MD) explores the time evolution of a system of atoms or molecules by solving Newton's equations of motion:

$$M_i \frac{d^2\mathbf{R}_i}{dt^2} = \mathbf{F}_i \tag{3.14}$$

where M_i is the mass of atom i, $\mathbf{R}_i$ is its position, and $\mathbf{F}_i$ is the net force acting on the atom. The forces are derived from the potential energy surface (PES) of the system. The Born–Oppenheimer Molecular Dynamics (BOMD) approach was employed in this thesis to perform molecular dynamics.[101] BOMD is based on the Born–Oppenheimer approximation. In BOMD, the electronic ground state is computed at each MD step by solving the Kohn–Sham equations of the Density Functional Theory (DFT) and the ionic forces are calculated using the Hellmann–Feynman theorem. The steps in a BOMD are:

(a) For atomic positions $\{\mathbf{R}_i(t)\}$, solve:

$$\hat{H}_{\mathrm{KS}}[\rho(\mathbf{r})]\psi_i(\mathbf{r}) = \epsilon_i\psi_i(\mathbf{r}) \tag{3.15}$$

to obtain the ground-state electron density $\rho(\mathbf{r})$ and the corresponding ground-state energy.

(b) Compute the forces on each ion using the Hellmann–Feynman theorem:

$$\mathbf{F}_i = -\frac{\partial E_{\mathrm{DFT}}}{\partial \mathbf{R}_i} \tag{3.16}$$

(c) Propagate the atomic positions using a suitable integrator, such as the Velocity-Verlet algorithm:

$$\mathbf{R}_i(t+\Delta t) = \mathbf{R}_i(t) + \mathbf{v}_i(t)\Delta t + \frac{1}{2}\frac{\mathbf{F}_i(t)}{M_i}(\Delta t)^2 \tag{3.17}$$

BOMD produces highly accurate trajectories because the potential energy surface is re-evaluated precisely at each step. However, this also makes it computationally expensive. There is another kind of ab initio molecular dynamics, called Car-Parrinello Molecular Dynamics (CPMD).[102] CPMD solves the electronic structure problem only once at the initial configuration and then propagates the electronic wavefunction forward in time using an extended Lagrangian scheme with fictitious electronic mass, thereby minimizing expensive self-consistent field iterations at each time step. However, CPMD requires smaller time steps to maintain stability of the electronic propagation.[76,102]

3.4.1 Nosé–Hoover thermostat

To model systems in the canonical (NVT) ensemble, it is necessary to control the temperature. In this thesis, temperature was regulated using the Nosé–Hoover thermostat, which introduces a fictitious variable ξ representing the coupling between the system and an external heat bath.[103,104]

The modified equations of motion are:

$$\frac{d\mathbf{R}_i}{dt} = \mathbf{v}_i \tag{3.18}$$

$$\frac{d\mathbf{v}_i}{dt} = \frac{\mathbf{F}_i}{M_i} - \xi\mathbf{v}_i \tag{3.19}$$

$$\frac{d\xi}{dt} = \frac{1}{Q}\left(\frac{\sum_i M_i v_i^2}{3Nk_BT} - 1\right) \tag{3.20}$$

Here, ξ is a dynamic friction coefficient that adjusts the system's kinetic energy. The parameter Q is analogous to a mass and controls the thermostat's response time.T denotes the target temperature. N is the number of atoms, and k_B is the Boltzmann constant.[105]

The thermal equilibrium is maintained by continuously exchanging kinetic energy with the thermostat variable. If the system's temperature rises above T, ξ becomes positive and decreases the velocities. If the temperature instead falls below T, ξ becomes negative and accelerates the atoms. The Nosé–Hoover thermostat ensures smooth evolution and realistic temperature fluctuations, preserving the dynamics of the system.

3.5 Microkinetic modelling

The microkinetic modeling in this thesis is based on the mean-field approach, which assumes that the system is homogeneous and that species are randomly distributed.[106] Moreover, there is no interaction between the adsorbed species. To analyze the kinetics of the reaction, we follow how coverages of the species change with time and temperature. Coverage, in this case, is the fraction of each species, which should sum to one. The time evolution of the surface coverages is obtained by solving a set of ordinary differential equations within the framework of a mean-field microkinetic model.[16]

$$\frac{d\theta_j}{dt} = \sum_i v_{ij} r_i \tag{3.21}$$

where θ_j is the fractional coverage of species j, v_{ij} is the stoichiometric coefficient of species j in the elementary reaction i, and r_i is the rate of i-th elementary reaction that depends on the coverages. In Paper I, SciPy is used to numerically solve the differential equations. The solver uses the Backward Differentiation Formula (BDF) method and integrates the differential equations. In all other papers, ode23s solver within MATLAB is used to integrate the differential equations numerically until steady-state is reached.

3.5.1 Adsorption and desorption rate constants

The rate constant for the adsorption of the species i is calculated using collision theory:[16]

$$k_{ads} = \frac{p_i s_0 A}{\sqrt{2\pi m k_B T}} \tag{3.22}$$

where p_i is the pressure of species i, s_0 is the sticking coefficient, A refers to the area of the largest 8-membered ring through which the molecule needs to pass, m is the mass of species i, and k_B is Boltzmann's constant and T is the temperature. Thermodynamic consistency is ensured by calculating the desorption rate constant from k_{ads} and the equilibrium constant:

$$k_{des} = \frac{k_{ads}}{K_{eq}} \tag{3.23}$$

3.5.2 Reaction rate constants

The rate constants for the surface reactions are calculated within the transition state theory.[107] Transition state theory is based on the following assumptions: (1) the product is formed via an activated complex (transition state) through a loose vibration, (2) the

transition state and the reactants of the elementary steps are in quasi-equilibrium. (3) Species that have passed the transition state from the initial state will immediately form the final state.[106] Hence, for an elementary reaction described by $R_{IS} \rightleftharpoons R_{TS} \rightarrow P$, the rate constant k is given by

$$k = \nu K \tag{3.24}$$

with ν denoting the crossing frequency at which species at the transition state convert to the final state and K is the equilibrium constant, which is defined as:

$$K = \frac{Z_{TS}}{Z_{IS}} \tag{3.25}$$

Here, Z_{TS} and Z_{IS} are the partition functions for the transition state and the initial state, respectively. The thermodynamic form of the transition state rate expression is given by:

$$k = \frac{k_B T}{h} \exp(\frac{\Delta S^{\ddagger}}{k_B}) \exp(-\frac{\Delta H^{\ddagger}}{k_B T}) \approx \frac{k_B T}{h} \exp(\frac{\Delta S^{\ddagger}}{k_B}) \exp(-\frac{\Delta E^{\ddagger}}{k_B T}) \tag{3.26}$$

where $\Delta H^{\ddagger}$ and $\Delta S^{\dagger}$ are the enthalpy and entropy change for the formation of the transition state from the reactants, respectively. As pV does not change along the reaction path, $\Delta H^{\ddagger}$ is approximated by $\Delta E^{\ddagger}$ (the zero-point corrected barrier of the elementary reaction).

3.5.3 Analysis of reaction kinetics

Order of reaction

One way to characterize a reaction is by examining the dependence of its rate on the concentrations or partial pressures of the reactants, which is expressed in terms of reaction orders. According to the rate law, the relationship between the rate and partial pressure of the component is given by[106]:

$$r \propto \prod_i p_i^{n_i} \tag{3.27}$$

The reaction order for a given component i, denoted n_i, can be determined by assessing how the natural logarithm of the rate of the reaction in the forward direction, r^+, changes with respect to the natural logarithm of the component's partial pressure p_i. This relationship is given by[108]:

$$n_i = \frac{\partial \ln r^+}{\partial \ln p_i}, \tag{3.28}$$

Apparent activation energy

In addition to assessing the effect of reactant partial pressures on the reaction rate through reaction orders, one can explore the impact of temperature by examining the apparent activation energy. The apparent activation energy is determined using the Arrhenius equation:

$$r = A \exp\left(-\frac{E_{\mathrm{a}}}{k_B T}\right) \prod_i p_i^{n_i} \tag{3.29}$$

where E_a represents the apparent activation energy, k_B is boltzmann constant, T is the temperature, p_i is the partial pressure of species i and n_i is the reaction order of species i.[106]

3.6 Calculating NMR signatures

Nuclear magnetic resonance (NMR) observables depend sensitively on the electronic distribution close to the nucleus, making an accurate reconstruction of the all-electron behaviour essential for reliable predictions.[109] In periodic DFT calculations, the Gauge-Including Projector Augmented Wave (GIPAW) method provides this accuracy by restoring the correct near-nucleus electronic currents and charge densities that are otherwise smoothed out by pseudopotentials.[110] Through this reconstruction, GIPAW enables the determination of key NMR parameters such as chemical shieldings, and electric field gradients.[111]

3.6.1 NMR chemical shielding and chemical shift

When an external magnetic field $\mathbf{B}_0$ is applied, electrons in the material generate an induced magnetic field $\mathbf{B}_{\text{ind}}$ that partially shields the nucleus. This response is described by the chemical shielding tensor $\boldsymbol{\sigma}$, defined as[110]

$$\sigma_{\alpha\beta}(A) = -\frac{\partial B_{\alpha}^{\text{ind}}(\mathbf{R}_A)}{\partial B_{\beta}}, \tag{3.30}$$

where $\mathbf{R}_A$ denotes the position of nucleus A. The isotropic shielding is the average of the three principal components:

$$\sigma_{\text{iso}} = \tfrac{1}{3}\left(\sigma_{xx} + \sigma_{yy} + \sigma_{zz}\right). \tag{3.31}$$

Experimentally, the chemical shift δ_{iso} is reported, which measures the shielding relative to a reference compound:

$$\delta_{\text{iso}}(A) = \sigma_{\text{ref}}(A) - \sigma_{\text{iso}}(A), \tag{3.32}$$

where σ_{ref} is the shielding constant of the reference compound such as tetramethylsilane (TMS) for ^{13}C or ^{1}H nuclei. $Al(NO_3)_3$ is conventionally used as the reference for ^{27}Al nuclei.

To relate the experimentally measured isotropic chemical shift (δ_{iso}) to the calculated isotropic chemical shielding (σ_{iso}) obtained from GIPAW, a linear regression is typically performed using a set of well-characterised reference compounds.[112] This procedure establishes relationship between calculated shieldings and observed shifts, which can be written in the general form, as shown in this Figure 3.2:

$$\delta_{\text{iso}} = a\,\sigma_{\text{iso}} + b,$$

where a and b are the slope and intercept obtained from the regression. These parameters depend on the chosen reference compounds.

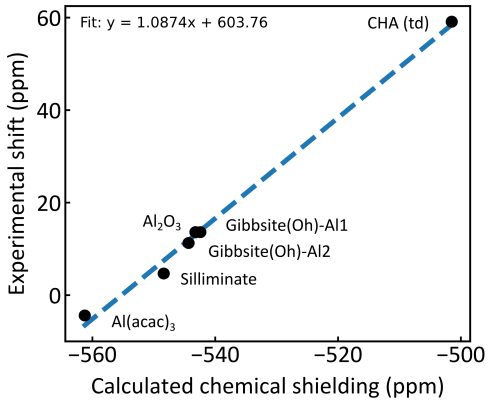

Figure 3.2: Linear regression between calculated isotropic shieldings (σ_{iso}) and experimental isotropic chemical shifts (δ_{iso}) for the reference compounds.

3.6.2 Quadrupolar coupling constant (C_Q) and asymmetry parameter (η)

For nuclei with spin $I \geq 1$, the nuclear quadrupole moment Q interacts with the electric field gradient (EFG) at the nucleus. The EFG tensor is given by the second derivatives of the electrostatic potential[109]:

$$V_{\alpha\beta}(A) = \left.\frac{\partial^2 V(\mathbf{r})}{\partial r_\alpha \partial r_\beta}\right|_{\mathbf{R}_A}, \tag{3.33}$$

Diagonalization of $V_{\alpha\beta}$ yields the principal components V_{xx}, V_{yy}, and V_{zz}, following the convention $|V_{zz}| \geq |V_{yy}| \geq |V_{xx}|$.

The quadrupolar coupling constant C_Q quantifies the magnitude of the interaction between the nuclear quadrupole moment Q and the electric field gradient (EFG) at the nucleus. It is defined as

$$C_q = \frac{eQV_{zz}}{h}, \tag{3.34}$$

where V_{zz} is the principal component of the EFG tensor, e is the elementary charge, and h is Planck's constant. A larger C_Q reflects a stronger quadrupolar interaction, indicating that the nucleus is highly sensitive to local structural distortions, electronic asymmetry, and deviations from ideal coordination geometry.

The asymmetry parameter η characterises the deviation of the EFG tensor from axial (cylindrical) symmetry. It is defined as

$$\eta = \frac{V_{xx} - V_{yy}}{V_{zz}}, \tag{3.35}$$

where V_{xx}, V_{yy}, and V_{zz} are the principal components of the EFG tensor. A value of $\eta = 0$ corresponds to a perfectly axially symmetric environment, typically associated with

high-symmetry coordination geometries, while values approaching $\eta = 1$ indicate strong distortion and the absence of symmetry. Together, C_Q and η provide detailed information on the local structural and electronic environment.

Chapter 4

Experimental Methods

In this chapter, a description of the experimental procedure used for NH_3-temperature-programmed desorption, NO temperature-programmed reaction, activity and selectivity measurement, and SO_2 uptake experiment are discussed.

All the measurements were performed using a plug flow reactor as shown in Figure 4.1. The inlet gas feed consisting of NH_3, NO, SO_2, and O_2 balanced with N_2 were regulated using mass flow controllers (Bronkhorst EL-FLOW), while water vapor was independently controlled and injected into the gas stream via a Controlled Evaporation and Mixing (CEM) system (Bronkhorst Hi-Tech), enabling precise control of water vapor concentration in the feed. The gas mixture could be directed either directly to the reactor or through a bypass line for baseline measurements. The catalyst bed (10–50 mg) was positioned in a quartz tube reactor and maintained at the desired temperature using a temperature controller and heating furnace. The outlet gas concentration was continuously monitored using a Fourier Transform Infrared (FTIR) spectrometer.

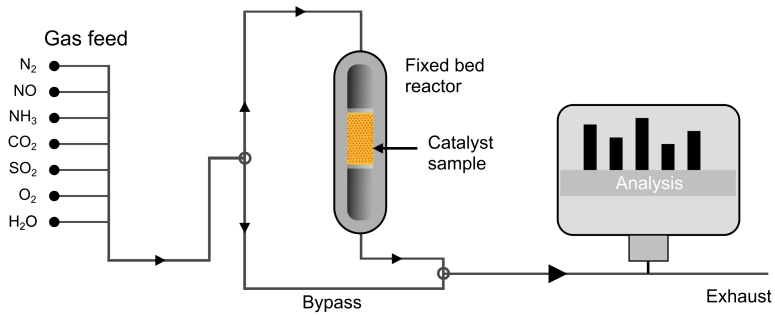

Figure 4.1: Representation of the flow reactor setup used in this work. Figure is adopted from ref.[113]

4.1 NH_3-temperature-programmed desorption

NH_3-temperature programmed desorption (NH_3-TPD) is a standard technique used to characterize the amount and type of acid sites in zeolites.[114,115] In the first step, NH_3 is adsorbed on the catalyst at low temperature, where it interacts with both Brønsted and Lewis acid sites. Under these conditions, NH_3 is assumed to saturate the accessible sites, forming either adsorbed NH_3 or ammonium species. The weakly physisorbed NH_3 is removed by exposing to H_2O and then purging with an inert carrier gas. The sample is

then heated using a constant heating rate. As the temperature increases, adsorbed NH_3 desorbs from the different sites. The desorption rate is typically recorded as a function of temperature and time.

The desorption of NH_3 during TPD in many cases follows the Polanyi–Wigner desorption rate expression:

$$r_{\mathrm{des}}(t) = -\frac{d\theta}{dt} = \nu\,\theta^n \exp\left(-\frac{E_{\mathrm{des}}}{k_B T}\right), \tag{4.1}$$

where r_{des} is the desorption rate, θ is the fractional coverage of NH_3, n is the desorption order (commonly $n = 1$ for NH_3), ν is the pre-exponential factor, E_{des} is the activation energy for desorption, k_B is the Boltzmann constant, and T is the temperature. For a linear heating ramp $T = T_0 + \beta t$, with a heating rate $\beta = dT/dt$, the desorption rate can also be expressed as:

$$r_{\mathrm{des}}(T) = -\beta\,\frac{d\theta}{dT} = \nu\,\theta^n \exp\left(-\frac{E_{\mathrm{des}}}{k_B T}\right). \tag{4.2}$$

This kinetic description connects the TPD signal to the strength of NH_3 adsorption, allowing the acid-site strength to be evaluated.

Procedure

The experiment involved mixing a 50 mg sample (sieve fraction of 150-300 μm) with 300 mg of SiC (mesh 60) and placing into a quartz U-tube reactor with a 6 mm inner diameter. Figure 4.2 shows the procedure followed for NH_3–TPD. The measurement began with pre-heating the sample at 500 °C in 10% O_2 to remove any adsorbed species or moisture. Next, at 100 °C, the sample was exposed to 1500 ppm NH_3, followed by exposure to 5% H_2O for 15 min to remove physisorbed NH_3, and an additional 60 min in dry N_2. Then the catalyst was cooled to 80 °C, to start the heating ramp to 550 °C, at a rate of 3 °C/min.

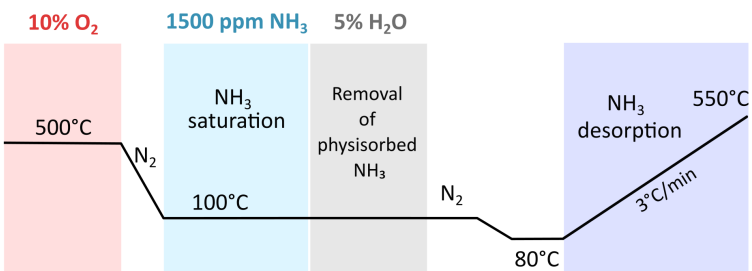

Figure 4.2: Procedure followed for NH_3–temperature programmed desorption.

Figure 4.3 shows a typical NH_3-TPD profile. Peaks at lower temperatures are associated with weakly bound NH_3 (weak acid sites), whereas desorption at higher temperatures corresponds to stronger acid sites. Quantitative analysis can be performed by integrating

the desorption signal over time to obtain the total amount of NH_3 desorbed (usually expressed in μmol NH_3 g^{-1} of catalyst).

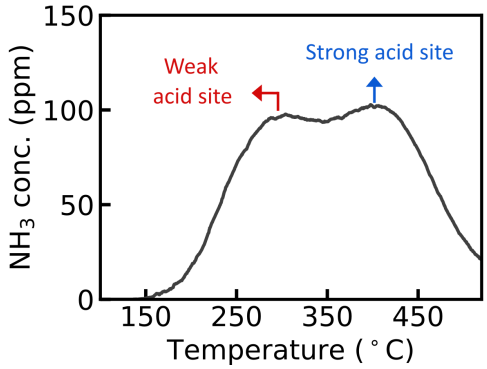

Figure 4.3: NH_3–temperature programmed desorption profile showing desorption from weak and strong acid sites.

In **papers III–V**, NH_3-temperature-programmed desorption (TPD) was used to quantify the Brønsted acid sites and to assess the deactivation due to dealumination in catalysts subjected to hydrothermal aging.

4.2 NO temperature-programmed reaction

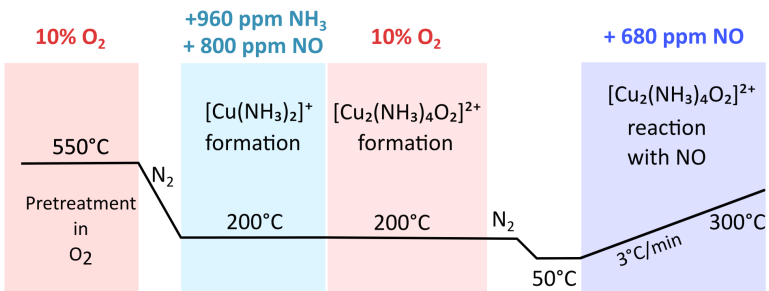

Figure 4.4: Procedure followed for NO–temperature programmed reaction on Cu-CHA catalyst.

NO temperature-programmed reaction (TP reaction) measurements were performed to probe the amount of $[Cu_2(NH_3)_4O_2]^{2+}$ species, which is a key intermediate formed in the NH_3-SCR over Cu-CHA catalyst.[116] The measurements were performed on 50 mg catalyst. Figure 4.4 shows the procedure followed for NO temperature-programmed reaction. The sample was prior the measurements heated to 10% O_2 at 550 °C. The pretreatment was followed by cooling the sample to 200 °C, where it was exposed to 800 ppm NO and 960 ppm NH_3, which results in $[Cu(NH_3)_2]^+$ complexes.[117] Subsequent oxidation at 200 °C in

10% O_2 yields $[Cu_2(NH_3)_4O_2]^{2+}$ complexes.[117,118] After the oxidation, the samples were cooled to 50 °C, and exposed to 680 ppm NO while heating from 50 to 300 °C at a rate of 3 °C/min. During heating, we monitored the consumption of NO from which the amount of $[Cu_2(NH_3)_4O_2]^{2+}$ [116] was estimated.

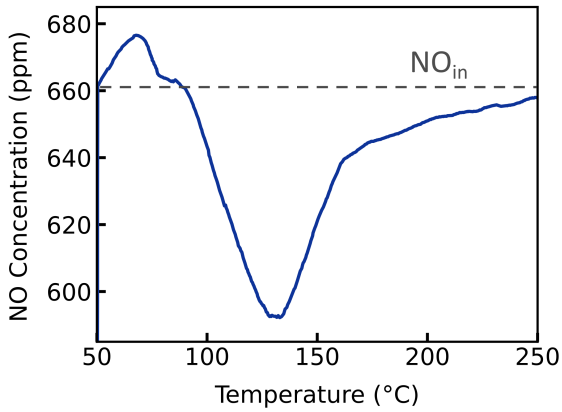

Figure 4.5: NO–temperature programmed reaction profile for Cu-CHA catalyst.

Figure 4.5 shows the NO temperature-programmed reaction profile obtained after experiment. At the experiment's onset, the catalyst contains $[Cu_2(NH_3)_4O_2]^{2+}$ complexes already formed by the procedure discussed earlier in this section. The sample is exposured to NO, but, at this low temperature, the $[Cu_2(NH_3)_4O_2]^{2+}$ complexes do not react with NO. As a result, the measured outlet NO concentration matches the inlet, indicating negligible reaction. As the temperature is increases, the system gain sufficient thermal energy for the reaction. This reaction can be seen as a drop in the outlet NO concentration in the figure 4.3. The rate at which this occurs can be expressed by a general temperature-programmed reaction rate equation:

$$\frac{d\alpha}{dT} = \frac{A}{\beta} \exp\left(-\frac{Ea}{k_B T}\right) f(\alpha), \tag{4.3}$$

Here, α can be defined as the fraction of $[Cu_2(NH_3)_4O_2]^{2+}$ that has reacted. The temperature dependent rate constant is given by

$$k(T) = A \exp\left(-\frac{Ea}{k_B T}\right), \tag{4.4}$$

which reflects the increasing reaction rate with temperature. The parameters A and Ea are the Arrhenius pre-exponential factor and apparent activation energy of the reaction, respectively. The function $f(\alpha)$ describes how the rate depends on the coverage of the reactant, while β is the programmed heating rate. The minimum in the curve, is observed at 130-140 °C, and corresponds to the peak reaction rate (maximum $d\alpha/dT$), where the combined effects of increasing temperature and remaining reactant availability are optimal. After 140 °C, most of the $[Cu_2(NH_3)_4O_2]^{2+}$ species have already been consumed,

the function $f(\alpha)$ decreases, which lowers the rate $(d\alpha/dT)$ and causes the outlet NO concentration to return toward the inlet level.

In **paper III**, NO-TP reaction measurements were carried out on fresh catalysts and samples hydrothermally aged for 2, 10, and 100 hours to investigate how hydrothermal aging affects the formation of $[Cu_2(NH_3)_4O_2]^{2+}$.[116] In **paper V**, NO-TP reaction measurements were performed to probe the amount of $[Cu_2(NH_3)_4O_2]^{2+}$ in fresh, hydrothermally aged, SO_2-exposure and regenerated catalyst enabling assessment of how each treatment influences the the formation of $[Cu_2(NH_3)_4O_2]^{2+}$.[116]

4.3 Activity and selectivity measurements

Catalytic activity is typically expressed as the rate at which reactants are converted under specified conditions. For the kinetic analysis, we used the common approximation that the NH_3-SCR reaction is first order in NO and zeroth order in NH_3 [119–121]. The rate constant k (mol/g h) can under these assumptions be evaluated as:

$$k = -\frac{F \ln(1 - X_{\mathrm{NO}})}{W} \tag{4.5}$$

where, F is the total molar flow (0.6027 mol/h), X_{NO} is the NO conversion, and W is the amount of catalyst (50 mg).

The selectivity of a catalyst is measured by the ratio of desired product to total products. In NH_3-SCR, selectivity refers to how much of the converted NO is transformed into N_2 rather than by-products such as N_2O.

$$S_{\mathrm{N_2O}} = \frac{\text{moles of } N_2O \text{ formed}}{\text{moles of NO converted}} \tag{4.6}$$

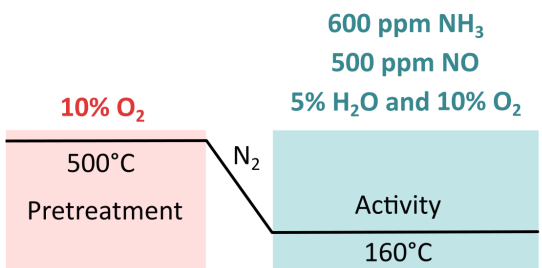

Figure 4.6: Procedure followed for activity measurement on Cu-CHA catalyst.

Activity measurements were performed using 50 mg of dry catalyst material in **papers III** and **V** for fresh and aged samples, while in **paper II** measurements were performed using 10 and 4 mg of sample for different temperature and partial pressure of H_2O, respectively. Figure 4.6 shows the procedure followed for activity measurement. The

catalyst was first pretreated with 10% O_2 at 500 °C. The catalyst was then exposed to a gas mixture containing 500 ppm NO, 600 ppm NH_3, 10% O_2, and 5% H_2O. The measurements were conducted at different temperatures in an N_2 carrier gas with a total flow rate of 13.5 NL/h. The concentrations of NO, NO_2, and N_2O were monitored using a Gasmet CX4000 FTIR spectrometer.

In **paper II**, activity measurements were carried out to evaluate the inhibitory effect of H_2O on the SCR reaction. The reaction rate constants were determined with respect to increasing H_2O partial pressure (0-25%). In **paper III**, the influence of hydrothermal aging on SCR activity was investigated by measuring the change in rate constant over fresh catalysts and samples aged for up to 100 hours, providing insight into hydrothermal deactivation mechanisms. In **paper V**, activity measurements were performed on fresh, hydrothermally aged, SO_2-exposure and regenerated catalyst to assess how hydrothermal aging influences SO_2-induced deactivation and the subsequent regeneration behaviour.

4.4 SO_2 uptake experiments

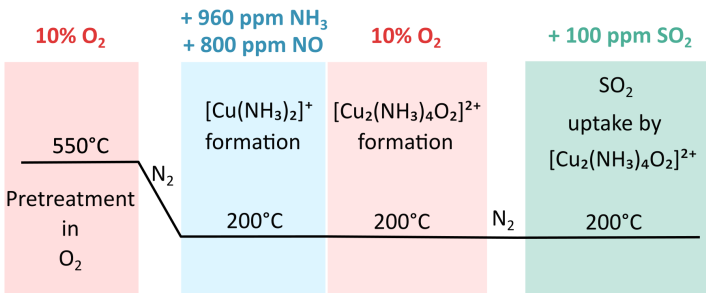

Figure 4.7: Procedure followed for SO_2 uptake experiments on Cu-CHA catalyst.

In **paper V**, SO_2-uptake experiments were conducted to measure how much SO_2 Cu-CHA can adsorb before it becomes saturated. This was done to understand the extent of sulfur poisoning in the catalyst. The overall procedure for SO_2 uptake experiments is shown in Figure 4.7. The sample was prior to the measurements heated to 10% O_2 at 550 °C. The pretreatment was followed by cooling the sample to 200 °C, where it was exposed to 800 ppm NO and 960 ppm NH_3, which results in $[Cu(NH_3)_2]^+$ complexes.[117] Subsequent oxidation at 200 °C in 10% O_2 yields $[Cu_2(NH_3)_4O_2]^{2+}$ complexes.[117,118] After the formation of the $[Cu_2(NH_3)_4O_2]^{2+}$ complexes, the SO_2 concentration in the feed gas was measured for 15 min by bypassing the reactor, to obtain a good background. The sample was then exposed to 100 ppm SO_2/N_2 for 45 minutes at 200 °C, during which the outlet SO_2 concentration decreased.[26] After 45 minutes, the outlet SO_2 concentration returned to the feed concentration, indicating the completion of SO_2 uptake. The resulting uptake profile is shown separately in Figure 4.8. The SO_2 uptake was then quantified by integrating the SO_2 consumption curve as a function of time, represented by the blue-shaded area in Figure 4.8.

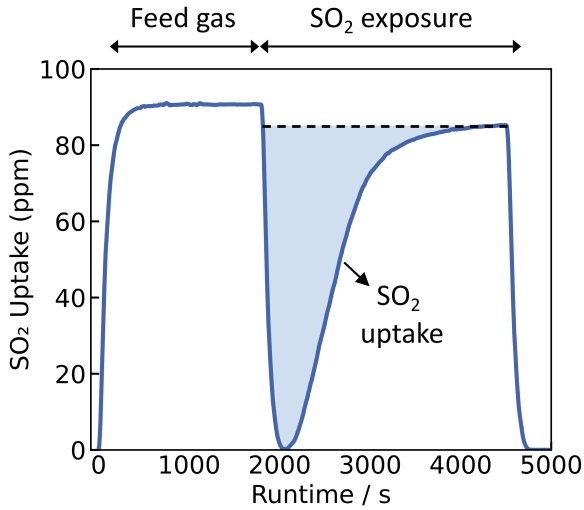

Figure 4.8: The SO_2 uptake of Cu-CHA during exposure to 100 ppm SO_2 in N_2 at 200 °C.

Chapter 5

Mechanistic understanding of Cu-CHA deactivation

Experimental measurements are in this thesis combined with density functional theory (DFT) calculations to provide detailed insights into the mechanisms of water inhibition, hydrothermal aging, and SO_2 poisoning. These processes alter the catalyst structure, Cu speciation, and activity of the NH_3-SCR reaction. Each deactivation pathway is associated with distinct stages of the NH_3-SCR reaction cycle. Therefore, to interpret these deactivation mechanisms effectively, it is essential to first establish a clear understanding of the fundamental NH_3-SCR reaction cycle over Cu-CHA catalysts.

A detailed reaction scheme has been proposed based on density functional theory (DFT) calculations and DFT-based microkinetic modeling.[55,56] Figure 5.1 shows a simplified version of the proposed reaction mechanism for standard NH_3-SCR. At temperatures below 300 °C, Cu ions are solvated by NH_3, forming mobile $[Cu(NH_3)_2]^+$ complexes.[57–60] Pairs of $[Cu(NH_3)_2]^+$ complexes (A) are essential for the adsorption and activation of O_2, a critical step in the NH_3-SCR reaction. Adsorption of O_2 on $[Cu(NH_3)_2]^+$ pair leads to the formation of a $[Cu_2(NH_3)_4O_2]^{2+}$ peroxo complex (B), which is a key intermediate in the reaction cycle.[61–63] The reaction proceeds via adsorption of NO on $[Cu_2(NH_3)_4O_2]^{2+}$ peroxo complex. However, NH_3 adsorption competes with NO adsorption and blocks the $[Cu_2(NH_3)_4O_2]^{2+}$ sites for the reaction to form $[Cu_2(NH_3)_5O_2]^{2+}$ (F) which is an inactive state of the catalyst, giving rise to the known negative reaction order of the NH_3-SCR reaction in NH_3.[56] Once, NO adsorbs over the $[Cu_2(NH_3)_4O_2]^{2+}$ peroxo complex, it reacts with NH_3 to form H_2NNO and $[Cu_2(NH_3)_4OOH]^{2+}$ (C). H_2NNO can diffuse away from the Cu sites and decompose over Brønsted acid sites to produce N_2 and H_2O[56,64]. Another H_2NNO can form over $[Cu_2(NH_3)_4OOH]^{2+}$ giving $[Cu_2(NH_3)_4OH]^{2+}$ (E) over which a second HONO can form. $[Cu_2(NH_3)_4OOH]^{2+}$ can reacts with NO and NH_3 to form $[Cu_2(NH_3)_4OHOH]^{2+}$ (D) with release of H_2NNO. $[Cu_2(NH_3)_4OHOH]^{2+}$ reacts with NO to form $[Cu_2(NH_3)_4OH]^{2+}$ and HONO. Each HONO formed in the main reaction cycle decompose together with NH_3 over Brønsted acid sites to N_2 and H_2O. The Brønsted acid sites are at reaction conditions occupied by NH_3 forming $NH_4{}^+$, thus H_2NNO and HONO are effectively decomposed over $NH_4{}^+$. An unwanted side-reaction is N_2O formation, which may occur if H_2NNO decomposes over $[Cu_2(NH_3)_4OOH]^{2+}$.[122] The selectivity of the reaction depends critically on the ratio between the barriers for H_2NNO diffusion, decomposition and the availability of Brønsted acid sites.[56] The proposed NH_3-SCR mechanism relies on both Cu sites and Brønsted acid sites to form N_2 and H_2O.[56]

When a catalyst is deactivated, the reaction can no longer proceed as it does on the fresh catalyst. This implies that the sites for the reaction have been modified or the reactants cannot access the sites. In the case of Cu-CHA, such modifications can affect

either the Cu sites or the Brønsted acid sites, leading to decrease in catalytic activity and performance.

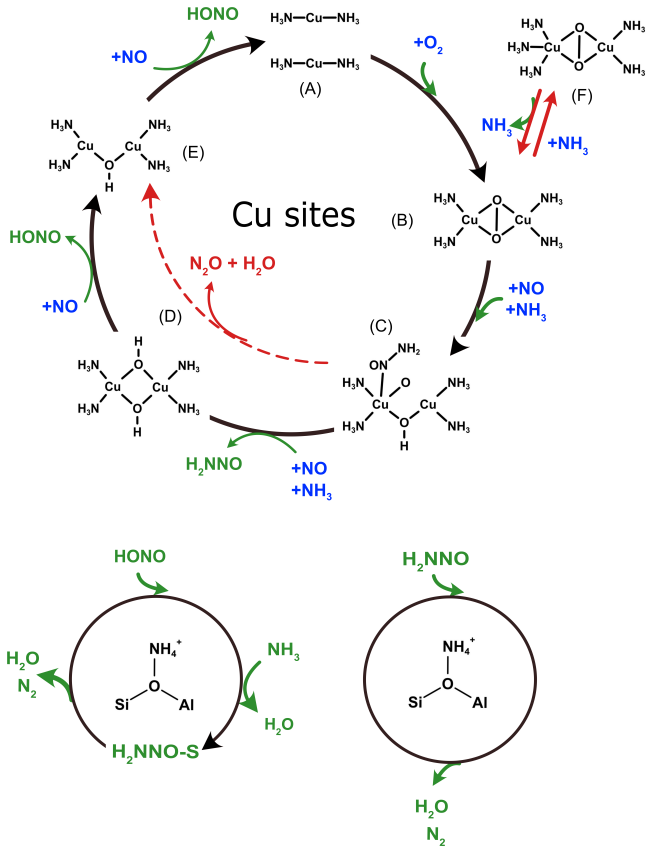

Figure 5.1: Simplified proposed reaction cycle for low-temperature NH_3-SCR over Cu-CHA.

5.1 Catalyst deactivation

Although Cu-CHA is the preferred catalyst for NO_x abatement, it suffer from deactivation during prolonged operating condition. Hydrothermal aging and SO_2 deactivation are primary deactivation processes that restrict the performance and stability of Cu-CHA.

During diesel particulate filter (DPF) regeneration, the exhaust system can reach temperatures around 650 °C. At these elevated temperatures, hydrothermal aging in the presence of water vapor can occur, leading to dealumination of the zeolite framework. The

dealumination process removes framework aluminum atoms, resulting in the formation of extra-framework aluminum species such as $Al(OH)_3(H_2O)$. Dealumination also causes a loss of Brønsted acid sites and induces structural distortion, both of which negatively affect catalytic activity and contribute to long-term catalyst degradation.[25,123,124] When the aging temperature or duration is further increased (for example, to 800 °C), dealumination becomes more extensive. Under such severe conditions, Cu-Al species[24,125,126] and CuO_x [127]aggregates can form, diminishing the number of active Cu sites necessary for the NH_3-SCR reaction. Additionally, both the Cu loading and the Si/Al ratio significantly influence hydrothermal stability. High Cu loadings have been found to accelerate structural deterioration compared to moderate loadings,[128] while catalysts with higher Si/Al ratios exhibit more pronounced dealumination and performance losses under aging conditions.[129]

Diesel fuel and lubricants contain trace levels of sulfur, which is oxidized to SO_2 and SO_3 during combustion. Even at low concentrations (tens of ppm), SO_2 has been shown to severely suppress the low-temperature NH_3-SCR activity of Cu-CHA, while the high-temperature window is much less affected.[130,131] SO_2 deactivation causes reversible and irreversible, which distinctly depend on chemical nature and thermal stabilities of the formed sulfur species. Reversible deactivation is not proportional to the sulfur content, and shows a strong deactivation already at low SO_2/Cu ratios.[27] Reversible SO_2 deactivation is mainly linked to the formation of less stable $(NH_4)HSO_4$ or $(NH_4)_2SO_4$. $(NH_4)HSO_4$ can restrict the inter-cage diffusion of $[Cu(NH_3)_2]^+$ and hinder O_2 activation, required for formation of $[Cu_2(NH_3)_4O_2]^{2+}$ peroxo complex.[132] Irreversible deactivation exhibits a strict 1:1 correlation between the extent of deactivation and the sulfur content.[27] Irreversible deactivation by SO_2 is mainly linked to interaction of SO_2 with the Cu sites and more specifically with the $[Cu_2(NH_3)_4O_2]^{2+}$ peroxo complex and Cu^{II} species in the presence of NH_3, as revealed by in-situ XANES measurements.[118] This interaction leads to a partial reduction of Cu^{II} to Cu^{I} and the formation of a Cu^{II}-sulfated compound, which is not reducible by NO/NH_3.[133] When the catalyst is regenerated by heating in O_2 at around 550 °C, the reversible part of the deactivation can be recovered through decomposition of $(NH_4)HSO_4$, $(NH_4)_2SO_4$ or weak Cu-bound sulfate species.[27,131,134] However, some strongly coordinated Cu–sulfate species can also form which remain intact even after regeneration at 550 °C, resulting in the irreversible deactivation.[134,135]

In this chapter, detailed insights are provided into (i) the effects of H_2O at low temperatures (H_2O inhibition) and high temperatures (hydrothermal aging), and (ii) the influence of hydrothermal aging on SCR activity, SO_2 deactivation, and catalyst regeneration.

5.2 Effect of H_2O at low temperatures

In **paper II**, the impact of high partial pressures of H_2O on low-temperature NH_3-SCR was investigated through combined experimental measurements and DFT-based microkinetic modeling. Figure 5.2 (a) shows the NO_x conversion at 200 °C over the catalyst decreases as the H_2O partial pressure increases from 2 to 25%, with the dry case also included for comparison. This trend clearly demonstrates the inhibitory effect of H_2O, where increasing H_2O partial pressure decreases the SCR activity under these conditions. At the same time, the apparent reaction order in H_2O decreases from −0.17

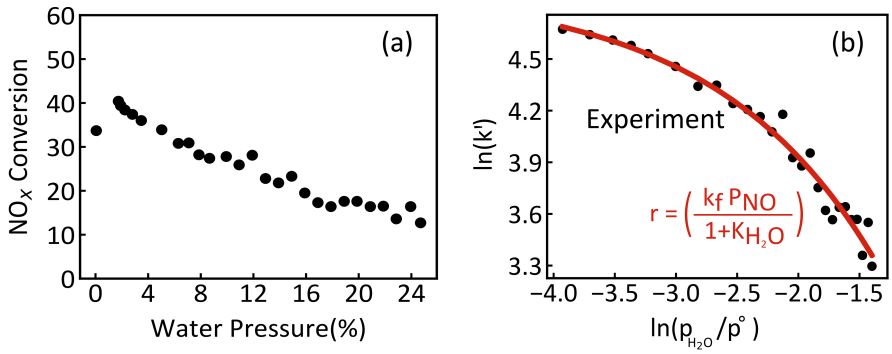

Figure 5.2: (a) NO conversion at 200 °C as a function of the partial pressure of H_2O was measured using 4 mg of catalyst, exposed to a gas mixture containing 500 ppm NO, 600 ppm NH_3, 10% O_2, and H_2O concentrations ranging from 2% to 25%, in an N_2 carrier gas with a total flow rate of 18 NL/h. and (b) Natural logarithm of the rate constant ($\ln k'$) as a function of the natural logarithm of the partial pressure of H_2O ($\ln(p_{H_2O}/p^\circ)$). The points represents experimental data, while the solid line corresponds to a fit based on a Langmuir-type expression.

to −1.18.

The inhibition of the reaction at high H_2O partial pressures arises from H_2O adsorption on key Cu intermediates in the reaction cycle. H_2O binds strongly to both the peroxo complex $[Cu_2(NH_3)_4O_2]^{2+}$ (B) and the $[Cu_2(NH_3)_4OHOH]^{2+}$ intermediate (D), thereby competing with NH_3 and NO for the same adsorption sites.The adsorption energy of H_2O on $[Cu_2(NH_3)_4O_2]^{2+}$ is calculated to be 0.79 eV, which is higher than adsorption energy of NO (0.70 eV) and is comparable to NH_3 adsorption (0.98 eV).

For the $[Cu_2(NH_3)_4OHOH]^{2+}$ intermediate (D), H_2O adsorption is 0.59 eV which is higher than NO adsorption (0.39 eV) and similar to NH_3 (0.66 eV). The adsorption energies for NO, H_2O and NH_3 indicate that H_2O, in similarity with NH_3, hinders NO adsorption on Cu sites and, thereby, reduce the overall SCR activity.

A DFT based microkinetic model was constructed to compare the experimental TOF with the simulated TOF. The simulated TOF matches with the experimental TOF when the the entropy penalty for H_2O adsorption is reduced and a pressure-dependent term in the Gibbs free energy of H_2O adsorption, accounting for adsorbate-adsorbate interactions is included in adsorption energies and entropies from DFT calculations. Based on the microkinetic model, we found the two H_2O-blocked configurations $[Cu_2(NH_3)_4O_2(H_2O)]^{2+}$ and $[Cu_2(NH_3)_4OHOH(H_2O)]^{2+}$ dominate at high H_2O partial pressures, a simple Langmuir-type of expression for the rate of N_2 formation is proposed:

$$r_{N_2} = \frac{k_f}{1 + K_{H_2O}} P_{NO}$$

where r_{N_2} is an effective reaction rate and K_{H_2O} an effective equilibrium constant for H_2O adsorption on the Cu-ions. This equation closely matches the experiments, as shown by the red line in Figure 5.2 (b).

5.3 Effect of H_2O at high temperatures

At elevated temperature, the catalyst is often exposed H_2O, which causes hydrothermal deactivation. Hydrothermal aging results in dealumination, whereby aluminum is removed from the zeolite framework, causing a loss of Brønsted acid sites and the formation of extra-framework aluminum species and silanol nests. The dealumination process occurs through sequential hydrolysis steps involving up to four H_2O molecules, as illustrated in Figure 5.3 (a). In each step, a single Al-O bond in the zeolite is hydrolyzed to the corresponding Al-OH and Si-OH in the framework. In the case of H-CHA, represented by structure (c) in Figure 5.3, the first hydrolysis step exhibits the highest effective barrier of 1.25 eV. The subsequent steps proceed with considerably lower barriers and ultimately lead to the formation of the extra-framework aluminum species $Al(OH)_3H_2O$ (EFAl), shown as structure (d) in Figure 5.3. Formation of this species is exothermic by –1.49 eV. This is discussed in detail in **paper I**.

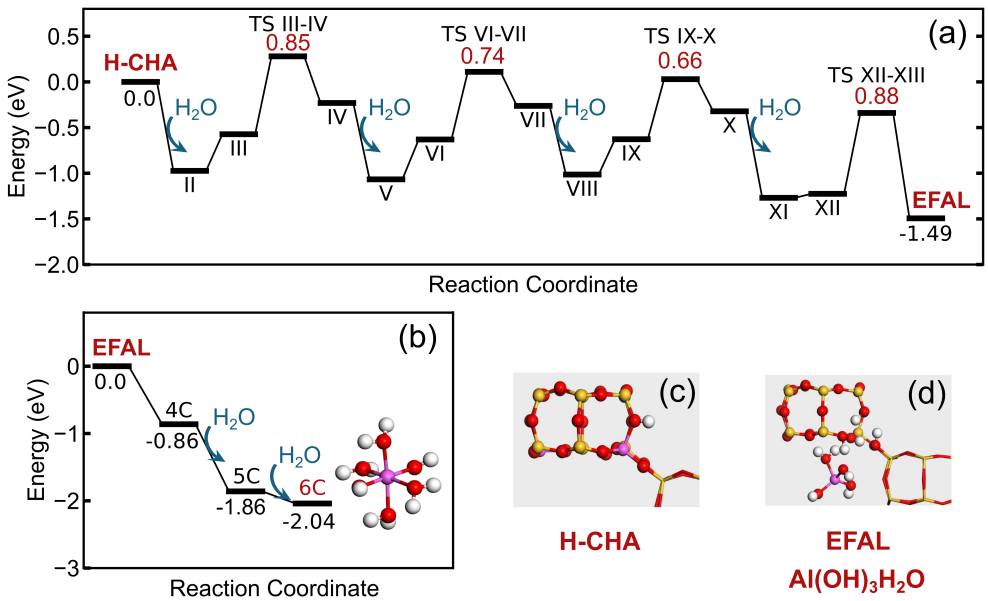

Figure 5.3: Potential energy landscape for (a) dealumination of H-CHA, (b) self-exchange reaction in H-CHA, (c) structure corresponding to H-CHA with a Brønsted acid sites, and (d) structure corresponding to $Al(OH)_3H_2O$ (EFAL).

The formed extra-framework Al species ($Al(OH)_3H_2O$) (EFAl) can transform to $[Al(OH)_2(H_2O)_2]^+$ (4C) via proton migration from neighbouring Brønsted acid sites as shown in Figure 5.3(b). This step is exothermic by -0.86 eV. Subsequent sequential addition of H_2O molecules results in $[Al(OH)_2(H_2O)_3]^+$ (5C) and $[Al(OH)_2(H_2O)_4]^+$ (6C), which is exothermic reactions, by -1.86 and -2.04 eV, respectively. The formation of

such charged octahedral species through this "self-exchange" reaction, results in additional loss of Brønsted acid sites. Thus, the loss of Brønsted acid sites measured from NH_3-temperature programmed desorption is due to dealumination and a self-exchange reaction. The occurance of such self-exchange is supported by solid state NMR and DFT-GIPAW calculations as discussed in **paper IV**.

Compared to H-CHA, Cu-CHA demonstrates significantly enhanced hydrothermal stability, commonly referred to as the Cu-CHA stabilization effect.[136] X-ray diffraction

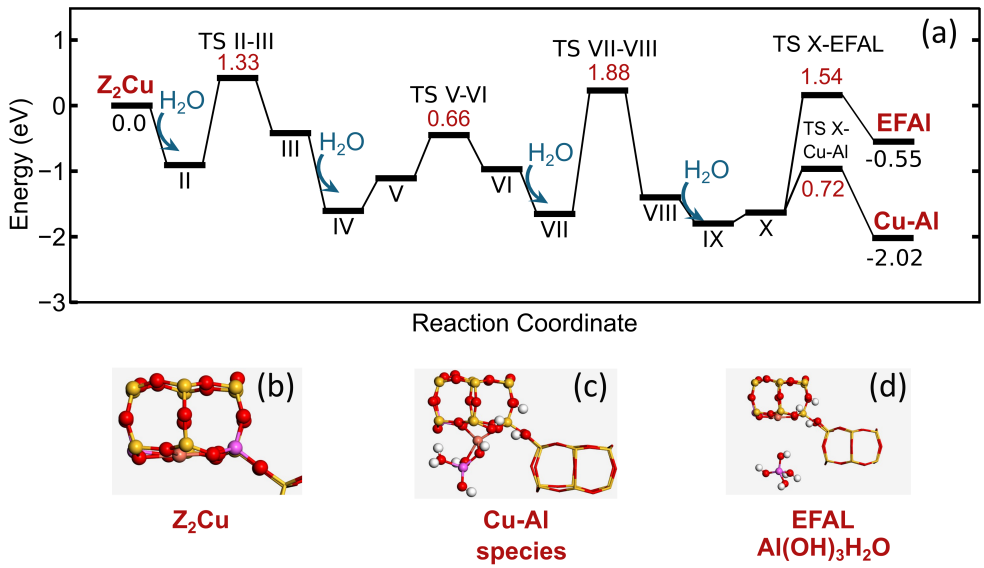

Figure 5.4: Potential energy landscape for (a) dealumination of Cu-CHA, and structure corresponding to (b) Z_2Cu, (c) Cu-Al species and (d) $Al(OH)_3H_2O$ (EFAL).

(XRD) measurements show that NH_4-CHA (the precursor to H-CHA) collapses at 850–900 K under hydrothermal conditions, whereas Cu-CHA remains stable up to 1100–1150 K.[136] Additionally, NH_3-temperature-programmed desorption (TPD) reveal a significantly loss of Brønsted acid sites in H-CHA compared to Cu-CHA. In Cu-CHA, the proton of H-CHA is replaced by Cu ions, which at high temperatures predominantly exist as Cu^{2+} in the Z_2Cu configuration, where Z denotes the anionic Al site in the zeolite framework.[124] In this configuration, the Cu ion resides in the plane of a six-membered ring and compensates the negative charge of two framework Al atoms. Z_2Cu species serves as the initial structure for dealumination, as illustrated in structure (b) of Figure 5.4. The dealumination process in Z_2Cu also proceeds through sequential hydrolysis steps, where up to four H_2O molecules react one after another to break the Al–O bonds in the framework as shown in Figure 5.4 (a). The four-step hydrolysis can lead either to the formation of a Cu–Al species that remains bound to the framework, shown as structure (c) in Figure 5.4, or to the formation of an extra-framework aluminum species, $Al(OH)_3H_2O$, shown as structure (d)

in Figure 5.4. Among the four steps, the third hydrolysis step has the highest barrier of 1.88 eV, while the fourth step determines whether $Al(OH)_3H_2O$ or a Cu–Al species forms. Formation of the extra-framework $Al(OH)_3H_2O$ species is exothermic by –0.55 eV and occurs with a barrier of 1.54 eV. In contrast, formation of the Cu–Al framework-bound species proceeds with a significantly lower barrier of 0.72 eV and is more exothermic, indicating that this pathway is both kinetically and thermodynamically preferred. The increased stability of Cu-CHA is therefore associated higher hydrolysis barriers for all four steps compared to those in H-CHA. Since these Cu–Al species remain bonded to the zeolite framework, their formation is likely reversible, contrasting with the irreversible dealumination involved in extra-framework aluminum formation. Hence, explaining the stabilization of framework by Cu in Cu-CHA, which is discussed in **paper I**.

5.4 Effect of hydrothermal aging on the reaction mechanism

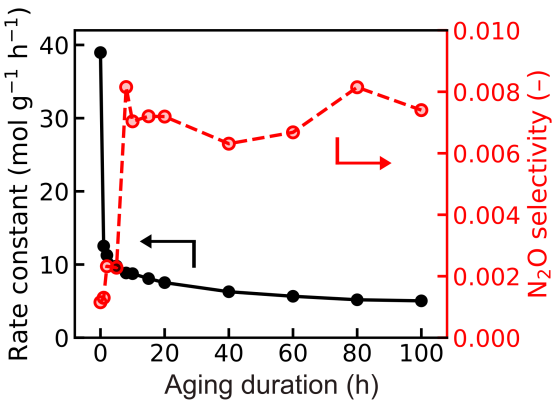

Figure 5.5: Rate constant ($mol\,g^{-1}\,h^{-1}$) for NO conversion and N_2O selectivity as a function of hydrothermal aging duration at 650 °C for 3.2 wt.% Cu-CHA (SAR 13.4).

The mechanism of NH_3–SCR over a catalyst subjected to hydrothermal deactivation was explored through experimental methods and DFT-based kinetic modeling in **paper III**. Figure 5.5 illustrates how the reaction rate constant varies with the aging duration, ranging from 0 to 100 hours. Initially, there is a decline in activity within the first 10 hours, referred to as fast deactivation, followed by a more gradual decline in the rate constant after 10 hours, referred to as slow deactivation. Thus, two types of deactivation processes were identified following hydrothermal aging. The initial rapid drop in activity aligns with a rise in N_2O selectivity, which remains relatively stable after 10 hours of aging. This suggested initial loss of the activity is related to Brønsted acid sites. NH_3-TPD measurement revealed most of the Brønsted acid sites were lost within first two hours of aging. Despite this, the catalyst still exhibits activity after hydrothermal aging. As Brønsted acid sites facilitate the decomposition of HONO and H_2NNO to N_2 and H_2O, their loss suggests that these reactions instead occur on alternative active sites, which

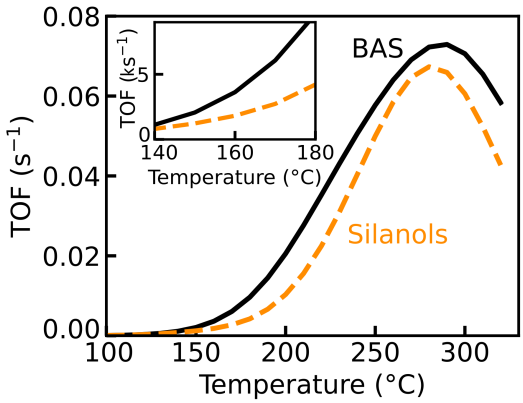

Figure 5.6: Simulated turnover frequency for NO conversion over Cu-CHA as a function of temperature over Brønsted acid sites (solid black line) and silanol-groups (dashed orange line). The inset shows a close up of the TOF from 140 °C to 180 °C.

can be silanol nests formed due to dealumination.

DFT-calculations showed that HONO and H_2NNO can decompose over silanol groups. However, the highest barrier for HONO and H_2NNO associated with a silanol groups is 0.59 eV compared to 0.38 eV over Brønsted acid sites. Indicating, the HONO and H_2NNO decomposition becomes slower over silanol nests.

Additionally, the loss of Brønsted acid sites also changes the Al distribution in the zeolite, which affects Cu sites. The NO-TPR experiments show that the amount of $[Cu_2(NH_3)_4O_2]^{2+}$ (B) complexes is reduced to 68% after 10 hours of aging and to 21% after 100 hours of aging. The reduced amount of formed $[Cu_2(NH_3)_4O_2]^{2+}$ complexes could originate from reduced stability and mobility of $[Cu(NH_3)_2]^{+}$ complexes and the formation of Cu-aluminate species, which are inactive for NH_3-SCR.

The kinetic effects when exchanging Brønsted acid sites with silanol groups for HONO and H_2NNO decomposition and a reduced number of paired $[Cu(NH_3)_2]^{+}$ complexes is studied based on DFT-based microkinetic modeling to calculate the rate of the entire NH_3-SCR cycle. The kinetic simulations showed that approximately half of the reduced activity after 100 hours of aging is connected to the loss of Brønsted acid sites as shown in the Figure 5.6, whereas the rest of the activity loss is related to reduced formation of $[Cu_2(NH_3)_4O_2]^{2+}$.

5.5 Impact of hydrothermal aging on SO_2 deactivation and regeneration

Deactivation by SO_2 and hydrothermal aging are two major deactivation mechanisms that limit the long-term performance and stability of Cu-CHA catalysts. Exposure to SO_2 in the exhaust stream can rapidly deactivate active Cu sites, hydrothermal aging prior to SO_2 exposure, further complicating SO_2 deactivation mechanism and regeneration

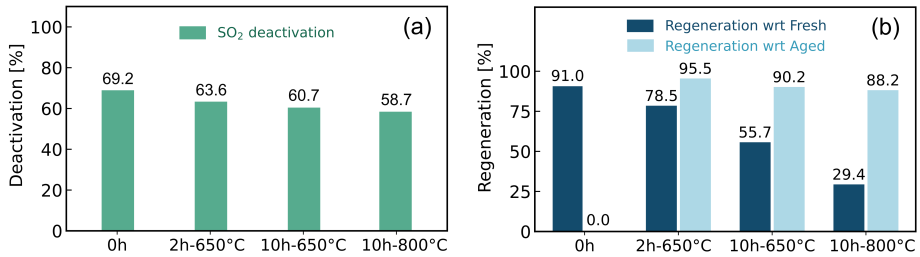

Figure 5.7: (a)Deactivation [%] by SO_2 and (b) Regeneration [%] with respect to fresh and aged under four aging conditions: 0 h, 2 h at 650 °C, 10 h at 650 °C, and 10 h at 800 °C.

behavior. In **paper V**, the impact of hydrothermal aging on SO_2 deactivation on Cu-CHA is studied. The experiments are conducted under four conditions: no aging (only SO_2 deactivation), aging at 650 °C for 2 hours, 650 °C for 10 hours, and 800 °C for 10 hours prior to SO_2 exposure followed by regeneration.

The fresh catalyst exhibited a 69% deactivation upon SO_2 exposure without aging, which slightly declined to 64%, 61%, and 59% when catalyst is aged at 650 °C for 2 h, 650 °C for 10 h, and 800 °C for 10 h prior to SO_2 exposure, respectively as shown in Figure 5.7 (a). The deactivation due to SO_2 decreases slightly with aging but the change is small. Thus, SO_2 deactivation appears largely independent of hydrothermal aging conditions. The slight decrease in SO_2 deactivation is explained by NO-TPR measurements which quantifies $[Cu_2(NH_3)_4O_2]^{2+}$ formation. Aging prior to SO_2 exposure, decreases $[Cu_2(NH_3)_4O_2]^{2+}$ formation, particularly under 800 °C for 10 hours conditions, suggesting that fewer $[Cu_2(NH_3)_4O_2]^{2+}$ sites are available for deactivation, leading to reduced SO_2 poisoning. Additionally, SO_2 uptake by $[Cu_2(NH_3)_4O_2]^{2+}$ decreases by approx 50% after 10 hours at 800 °C. Hence, confirming the reduced formation of $[Cu_2(NH_3)_4O_2]^{2+}$.

Figure 5.7 (b) shows regeneration at 550 °C restored up to 91% of activity in the catalyst exposed to SO_2 without aging but achieved only 30% recovery in catalysts aged at 800 °C for 10h prior to SO_2 exposure. This decrease in regeneration is due to irreversible loss of loss of Brønsted acid sites and reduced ability of catalyst to form $[Cu_2(NH_3)_4O_2]^{2+}$. The reduced regeneration is mainly due to irreversible deactivation caused by hydrothermal aging, along with an additional 5–10% irreversible loss associated with SO_2 exposure, light blue bar in Figure 5.7 (b).

Chapter 6

Conclusions and outlook

The main objective of this thesis has been to investigate the deactivation mechanisms of the Cu-CHA catalyst for NH_3-SCR, specifically focusing on water inhibition, hydrothermal aging, and sulfur poisoning under various temperature and pressure conditions. These were addressed by combining experimental methods with Density Functional Theory (DFT) calculations and a DFT-based microkinetic model.

The speciation of Cu is temperature-dependent. At low temperatures, Cu is solvated by NH_3, predominantly forming $[Cu(NH_3)_2]^+$ complexes, whereas at higher temperatures Cu is framework-bound, favoring the Z_2Cu and ZCuOH configuration. Accordingly, the thesis is structured into two main parts: (i) the effect of H_2O at low temperatures (H_2O inhibition) and high temperatures (hydrothermal aging), and (ii) the influence of hydrothermal aging on SCR activity, SO_2 deactivation, and catalyst regeneration.

At low temperatures (200 °C), the impact of high H_2O partial pressures on Cu-CHA catalysts was evaluated. H_2O was found to exhibit an inhibitory effect similar to that of NH_3, as evidenced by an increasingly negative reaction order with increasing H_2O partial pressure. This behavior was captured by a simple empirical expression. DFT calculations showed that H_2O compete with NO and NH_3 for adsorption on the Cu sites of $[Cu_2(NH_3)_4O_2]^{2+}$ and $[Cu_2(NH_3)_4OHOH]^{2+}$ complexes, providing a atomic-level understanding for the experimentally observed reaction inhibition.

At high temperatures, H_2O interacts with framework Al and causes dealumination of the zeolite. The stabilizing effect of Cu on the CHA framework was investigated by comparing the dealumination mechanism for H-CHA and Cu-CHA. Cu-CHA showed higher hydrolysis barriers for all four steps, involved in dealumination, compared with H-CHA. Cu–Al formation was preferred kinetically and thermodynamically over $Al(OH)_3H_2O$. The Cu–Al species remained bound to the framework and likely reversible, providing a mechanistic explanation for the stabilizing effect of Cu. Microkinetic modelling revealed the rate of dealumination significantly reduced in the presence of Cu. Additionally, dealumination was found to be sensitive to Al distribution.

In addition to understanding the dealumination mechanism, dealumination in H-CHA was quantified using NH_3-TPD and ^{27}Al and ^{29}Si NMR. NH_3-TPD overestimated the loss of Brønsted acid sites when compared with ^{27}Al and ^{29}Si NMR measurements, which quantifies the framework tetrahedral Al. It was found that $Al(OH)_3H_2O$ formed in dealuminated H-CHA, accepts a proton from neighbouring Brønsted acid sites via a "self-exchange" process to form a charged octahedral Al species, which result in additional loss of Brønsted acid sites without removal of framework. The self-exchange process revealed that the Brønsted acid site loss measured by NH_3-TPD corresponds to dealumination and self-exchange process. This improved our understanding of how loss of Brønsted acid site in NH_3-SCR should be interpreted.

Hydrothermal aging also influences the low-temperature NH_3-SCR mechanism. Two deactivation regimes were observed: a rapid initial deactivation linked to loss of Brønsted acid sites, followed by a slower deactivation associated with suppressed formation of the $[Cu_2(NH_3)_4O_2]^{2+}$ complex. DFT calculations showed that, in the aged catalyst, the decomposition of HONO and H_2NNO occurs over silanol groups rather than Brønsted acid sites, however, with higher barriers and consequently slower rates. A microkinetic model predicted that 50% of the activity loss originates from the decrease in Brønsted acid sites, and that the remaining loss is linked to a reduced amount of $[Cu_2(NH_3)_4O_2]^{2+}$.

The effect of hydrothermal aging on SO_2 deactivation was also investigated. Hydrothermal aging prior to SO_2 exposure slightly decreases the overall extent of SO_2-induced deactivation, while the fraction of irreversible deactivation remains essentially unchanged (within 5–10%). Thus, SO_2 deactivation was found to be largely independent of hydrothermal aging. The reduced deactivation was associated to decreased formation of the $[Cu_2(NH_3)_4O_2]^{2+}$ species, resulting in fewer sites available for SO_2 poisoning. Moreover, aging prior to SO_2 exposure also reduced the regeneration ability of the catalyst mainly due to irreversible caused by hydrothermal aging, along with an additional 5–10% irreversible deactivation associated with SO_2 exposure.

While this study has improved our understanding of the deactivation mechanism for NH_3-SCR over Cu-CHA catalysts, it still has certain limitations. The effect of high partial pressures of H_2O on the SCR performance was examined, whereas the promotional aspects of H_2O and H_2O-induced changes in Cu mobility and speciation were not addressed. The microkinetic model developed to capture observed inhibitory effect of H_2O successfully reproduces the experimental findings, although this required certain adjustments. In particular, the entropies of the blocked states were reduced to match experimental behavior, solely based on increased adsorbate–adsorbate interactions at high H_2O coverage. The model also assumes an NO:Cu of 2 NO per Cu site. Although experimental studies often suggest an NO:Cu of 1 NO per Cu site, the exact relationship remains uncertain. Despite good agreement with experiment, this simplification leaves scope for further model improvement.

In the microkinetic model used to describe the SCR rate over the aged catalyst (paper III), Brønsted acid sites were replaced with silanol groups. The effects of extraframework aluminum (EFAL) species present within the zeolite cage, along with the changes in aluminum distribution during hydrothermal aging, were not incorporated in the model. This simplified approach, while useful for capturing SCR rates for the fully hydrothermal aged catalyst, limited the ability of the model to predict rates under varying aging conditions and leaves scope for further improvement in this model.

Future research should focus on key aspects to further improve the mechanistic understanding of catalyst deactivation. A study examining the influence of H_2O concentrations on both SO_2 poisoning and dealumination mechanisms would be valuable. Additionally, the formation of charged octahedral species via self-exchange reactions in the zeolite may affect multiple deactivation pathways, including hydrothermal aging, sulfur poisoning, and overall SCR activity and should be studied. Finally, the SCR mechanism of aged catalysts was examined only at low temperature in this work. Extending this study to a broader temperature range and varying Si/Al ratios should significantly improve our understanding of the catalyst under more realistic operating conditions.

This work provides mechanistic insights into how H_2O under varying conditions and SO_2 deactivation affects catalyst stability and activity, linking these effects to the availability and speciation of both Cu sites and Brønsted acid sites. In doing so, it establishes the understanding necessary to improve the durability of Cu-CHA catalysts under dynamic automotive exhaust aftertreatment system, including variations in temperatures and H_2O partial pressures. These findings advance our understanding of the materials properties that control catalyst performance and provide a basis for designing more durable SCR catalysts with enhanced resistance to hydrothermal aging and sulfur poisoning.

Acknowledgments

The research was carried out at the Division of Chemical Physics and Competence Centre for Catalysis at Chalmers University of Technology, Göteborg, Sweden and at Umicore Denmark ApS, Hørsholm, Denmark in the period February 2022 to January 2026.

The research was funded by the European Union's Horizon 2020 research and innovation program under the Marie Sklodowska-Curie grant agreement no 955839 (CHASS).

The Competence Centre for Catalysis is hosted by Chalmers University of Technology, and financially supported by the Swedish Energy Agency, and the member companies: Volvo Group, Johnson Matthey, Perstorp, Powercell, Preem, Scania CV, and Umicore.

Computational time was granted by NAISS at NSC (Linköping) and PDC (Stockholm).

Additionally I would like to acknowledge the following people:

I would like to express my sincere gratitude to my main supervisors, Henrik Grönbeck and Ton V. W. Janssens, for their guidance, patience, and continuous support throughout this work. I am especially thankful for your availability for discussions and the time you consistently dedicated to our regular meetings.

I would also like to thank my co-supervisor Anders Hellman and examiner Magnus Skoglundh for their valuable discussions, insightful advice, and constructive feedback.

I am grateful to all members of the CHASS project for the stimulating discussions and encouragement during presentations and meetings.

I would like to acknowledge all my colleagues at Chemical Physics, KCK, and Umicore for creating such a friendly, supportive, and inspiring working environment.

I am deeply thankful to my friends in India and here, especially Ankita and David, for their constant support and the many enjoyable moments we shared. I am also grateful to Rahul for all the good times in Gothenburg. I would also like to thank Paul and Camilla for their constant encouragement.

Finally, and most importantly, I would like to thank my parents and my brother for their unconditional love, encouragement, and support throughout my life.

Bibliography

[1] Twigg, M. V. Progress and future challenges in controlling automotive exhaust gas emissions. *Appl. Catal. B: Environ.*, *70* (2007), 2–15.

[2] ACEA. Trucks: What They Are and Why They Are So Important (Fact Sheet). https://www.acea.auto/fact/trucks-what-they-are-and-why-they-are-so-important/, 2025. Accessed 2025-12-01.

[3] ACEA. Vehicles in Use – Europe 2023. https://www.acea.auto/files/ACEA-report-vehicles-in-use-europe-2023.pdf, 2023. Accessed 2025-12-01.

[4] Casper, J. K. *Fossil fuels and pollution: the future of air quality.* Infobase Publishing, 2010.

[5] European Environment Agency. Emissions of air pollutants from transport in Europe — Indicators. Technical report, European Environment Agency, 2025. URL https://www.eea.europa.eu/en/analysis/indicators/emissions-of-air-pollutants-from, accessed: 2025-10-24.

[6] World Health Organization. Health risks from transport and air pollution, 2020. URL https://www.who.int/teams/environment-climate-change-and-health/healthy-urban-environments/transport/health-risks, accessed: 2025-10-24.

[7] European Environment Agency. Harm to human health from air pollution in Europe: burden of disease status, 2024. Technical report, European Environment Agency, 2024. URL https://www.eea.europa.eu/en/analysis/publications/harm-to-human-health-from-air-pollution-2024, accessed: 2025-10-24.

[8] Wikipedia contributors. European emission standards, 2025. URL https://en.wikipedia.org/wiki/European_emission_standards, accessed: December 8, 2025.

[9] European Commission. Euro 7: The new emission standard for light and heavy-duty vehicles. Technical report, European Commission, 2024. URL https://theicct.org/wp-content/uploads/2024/03/ID-116-%E2%80%93-Euro-7-standard_final.pdf, accessed: 2025-10-24.

[10] Johnson, T. V. Diesel emission control in review. *SAE Transactions*, (2001), 128–144.

[11] Granger, P. and Parvulescu, V. I. Catalytic NO x abatement systems for mobile sources: from three-way to lean burn after-treatment technologies. *Chem. Rev.*, *111* (2011), 3155–3207.

[12] Rood, S.; Eslava, S.; Manigrasso, A.; and Bannister, C. Recent advances in gasoline three-way catalyst formulation: A review. *Proceedings of the Institution of Mechanical Engineers, Part D: Journal of Automobile Engineering*, *234* (2020), 936–949.

[13] Majewski, W. A. Diesel Filter Regeneration, 2022. URL `https://dieselnet.com/tech/dpf_regen.php`, accessed: 2025-12-01.

[14] Nova, I. and Tronconi, E. *Urea-SCR Technology for DeNO$_x$ After Treatment of Diesel Exhausts*. Springer Science+Business Media New York, 2014.

[15] Mohan, S.; Dinesha, P.; and Kumar, S. NOx reduction behaviour in copper zeolite catalysts for ammonia SCR systems: A review. *Chem. Eng. J.*, *384* (2020), 123253.

[16] Chorkendorff, I. and Niemantsverdriet, J. W. *Concepts of modern catalysis and kinetics*. John Wiley & Sons, 2017.

[17] Smith, J. K. History of catalysis. *Encyclopedia of catalysis*, (2002).

[18] Dumesic, J. A.; Huber, G. W.; and Boudart, M. Principles of Heterogeneous Catalysis. In Handbook of Heterogeneous Catalysis. (2008), 1–26.

[19] Brandenberger, S.; Kröcher, O.; Tissler, A.; and Althoff, R. The state of the art in selective catalytic reduction of NOx by ammonia using metal-exchanged zeolite catalysts. *Catal. Rev.*, *50* (2008), 492–531.

[20] Sun, Q.; Gao, Z.-X.; Chen, H.-Y.; and Sachtler, W. M. Reduction of NOx with ammonia over Fe/MFI: reaction mechanism based on isotopic labeling. *J. Catal.*, *201* (2001), 89–99.

[21] Zhang, D. and Yang, R. T. N2O formation pathways over zeolite-supported Cu and Fe catalysts in NH3-SCR. *Energy & fuels*, *32* (2018), 2170–2182.

[22] Madia, G. S. *Measures to enhance the NOx conversion in urea-SCR systems for automotive applications*. Ph.D. thesis, ETH Zurich, 2002.

[23] Nellessen, A. *Titania supported vanadium oxide catalysts in the NH3-SCR reaction: Effect of vanadium loading, promoters and aging*. Chalmers Tekniska Hogskola (Sweden), 2023.

[24] Singh, S.; Janssens, T. V.; and Grönbeck, H. Mechanism for Cu-enhanced hydrothermal stability of Cu–CHA for NH 3-SCR. *Catal. Sci. Technol.*, *14* (2024), 3407–3415.

[25] Gao, F. and Szanyi, J. On the hydrothermal stability of Cu/SSZ-13 SCR catalysts. *Appl. Catal. A: Gen.*, *560* (2018), 185–194.

[26] Abasabadi, R. K.; Janssens, T. V.; and Berlier, G. A quantitative analysis of the impact of SO 2 on the activity of Cu-CHA catalysts for NH 3-SCR. *Catal. Sci. Technol.*, *15* (2025), 5066–5075.

[27] Hammershøi, P. S.; Jangjou, Y.; Epling, W. S.; Jensen, A. D.; and Janssens, T. V. Reversible and irreversible deactivation of Cu-CHA NH3-SCRcatalysts by SO2 and SO3. *Appl. Catal. B: Environ.*, *226* (2018), 38–45.

[28] Bauerie, G.; Wu, S.; and Nobe, K. Reduction of nitric oxide with ammonia on noble metal catalysts. *Ind. Eng. Chem. Prod. Res. Dev.*, *14* (1975), 123–130.

[29] Inomata, M.; Miyamoto, A.; and Murakami, Y. Mechanism of the reaction of NO and NH3 on vanadium oxide catalyst in the presence of oxygen under the dilute gas condition. *J. Catal.*, *62* (1980), 140–148.

[30] Kato, A.; Matsuda, S.; Nakajima, F.; Imanari, M.; and Watanabe, Y. Reduction of nitric oxide with ammonia on iron oxide-titanium oxide catalyst. *J. Phys. Chem.*, *85* (1981), 1710–1713.

[31] Williamson, W. B. and Lunsford, J. H. Nitric oxide reduction with ammonia over copper (II) Y zeolites. *J. Phys. Chem.*, *80* (1976), 2664–2671.

[32] Seiyama, T.; Arakawa, T.; Matsuda, T.; Takita, Y.; and Yamazoe, N. Catalytic activity of transition metal ion exchanged Y zeolites in the reduction of nitric oxide with ammonia. *J. Catal.*, *48* (1977), 1–7.

[33] Jabłońska, M. Progress on noble metal-based catalysts dedicated to the selective catalytic ammonia oxidation into nitrogen and water vapor (NH3-SCO). *Molecules*, *26* (2021), 6461.

[34] Hansen, T. K. Development of new diesel oxidation and NH3 slip catalysts. (2017).

[35] Lan, T.; Zhao, Y.; Deng, J.; Zhang, J.; Shi, L.; and Zhang, D. Selective catalytic oxidation of NH 3 over noble metal-based catalysts: state of the art and future prospects. *Catal. Sci. Technol.*, *10* (2020), 5792–5810.

[36] Jansson, J. Vanadia-based catalysts for mobile SCR. In *Urea-SCR technology for deNOx after treatment of diesel exhausts*, pages 65–96. Springer, 2014.

[37] Lietti, L.; Alemany, J.; Forzatti, P.; Busca, G.; Ramis, G.; Giamello, E.; and Bregani, F. Reactivity of V2O5-WO3/TiO2 catalysts in the selective catalytic reduction of nitric oxide by ammonia. *Catal. Today*, *29* (1996), 143–148.

[38] Chen, H.; Xia, Y.; Fang, R.; Huang, H.; Gan, Y.; Liang, C.; Zhang, J.; Zhang, W.; and Liu, X. The effects of tungsten and hydrothermal aging in promoting NH3-SCR activity on V2O5/WO3-TiO2 catalysts. *Appl. Surf. Sci.*, *459* (2018), 639–646.

[39] Madia, G.; Elsener, M.; Koebel, M.; Raimondi, F.; and Wokaun, A. Thermal stability of vanadia-tungsta-titania catalysts in the SCR process. *Appl. Catal. B: Environ.*, *39* (2002), 181–190.

[40] Suarez-Corredor, A. F.; Babler, M. U.; Olsson, L.; Skoglundh, M.; and Westerberg, B. Characterization method for gas flow reactor experiments—NH3 adsorption on vanadium-based SCR catalysts. *Ind. Eng. Chem. Res*, *60* (2021), 11399–11411.

[41] Ye, B.; Jeong, B.; Lee, M.-j.; Kim, T. H.; Park, S.-S.; Jung, J.; Lee, S.; and Kim, H.-D. Recent trends in vanadium-based SCR catalysts for NOx reduction in industrial applications: stationary sources. *Nano Converg.*, *9* (2022), 51.

[42] An, X.; Feng, C.; Liu, J.; Cheng, G.; Du, Y.; Fan, Z.; and Wu, X. Insight into the sulfur resistance of manganese oxide for NH3-SCR: Perspective from the valence state distributions. *Appl. Surf. Sci.*, *592* (2022), 153223.

[43] Gevers, L. E.; Enakonda, L. R.; Shahid, A.; Ould-Chikh, S.; Silva, C. I.; Paalanen, P. P.; Aguilar-Tapia, A.; Hazemann, J.-L.; Hedhili, M. N.; Wen, F.; et al. Unraveling the structure and role of Mn and Ce for NOx reduction in application-relevant catalysts. *Nat. Commun.*, *13* (2022), 2960.

[44] Fang, X.; Liu, Y.; Cheng, Y.; and Cen, W. Mechanism of Ce-modified birnessite-MnO2 in promoting SO2 poisoning resistance for low-temperature NH3-SCR. *ACS Catal.*, *11* (2021), 4125–4135.

[45] Zhu, L.; Yao, J.; Ma, G.; Cao, P.; Wu, S.; and Li, Z. NH3-SCR performance and SO2 resistance comparison of CeO2 based catalysts with Fe/Mo additive surface decoration. *Chem. Eng. J.*, *428* (2022), 131372.

[46] Čejka, J.; Morris, R.; and Nachtigall, P. *Zeolites in Catalysis: Properties and Applications*. Royal Society of Chemistry, 2017.

[47] Davis, M. E. Ordered porous materials for emerging applications. *Nature*, *417* (2002), 813–821.

[48] Davis, M. E. and Lobo, R. F. Zeolite and molecular sieve synthesis. *Chem. Mater.*, *4* (1992), 756–768.

[49] Xin, Y.; Li, Q.; and Zhang, Z. Zeolitic materials for DeNOx selective catalytic reduction. *ChemCatChem*, *10* (2018), 29–41.

[50] Beale, A. M.; Gao, F.; Lezcano-Gonzalez, I.; Peden, C. H.; and Szanyi, J. Recent advances in automotive catalysis for NO x emission control by small-pore microporous materials. *Chem. Soc. Rev.*, *44* (2015), 7371–7405.

[51] Putluru, S. S. R.; Schill, L.; Jensen, A. D.; and Fehrmann, R. S. Selective catalytic reduction of NOx with NH3 on Cu-, Fe-, and Mn-zeolites prepared by impregnation: comparison of activity and hydrothermal stability. *J. Chem.*, *2018* (2018), 8614747.

[52] Shi, X.; Liu, F.; Xie, L.; Shan, W.; and He, H. NH3-SCR performance of fresh and hydrothermally aged Fe-ZSM-5 in standard and fast selective catalytic reduction reactions. *Environ. Sci. Technol.*, *47* (2013), 3293–3298.

[53] Kwak, J. H.; Tonkyn, R. G.; Kim, D. H.; Szanyi, J.; and Peden, C. H. Excellent activity and selectivity of Cu-SSZ-13 in the selective catalytic reduction of NOx with NH3. *J. Catal.*, *275* (2010), 187–190.

[54] Han, J.; Wang, A.; Isapour, G.; Harelind, H.; Skoglundh, M.; Creaser, D.; and Olsson, L. N2O formation during NH3-SCR over different zeolite frameworks: effect of framework structure, copper species, and water. *Ind. Eng. Chem. Res.*, *60* (2021), 17826–17839.

[55] Chen, L.; Janssens, T. V.; Vennestrøm, P. N.; Jansson, J.; Skoglundh, M.; and Grönbeck, H. A complete multisite reaction mechanism for low-temperature NH3-SCR over Cu-CHA. *ACS Catal.*, *10* (2020), 5646–5656.

[56] Feng, Y.; Wang, X.; Janssens, T. V.; Vennestrøm, P. N.; Jansson, J.; Skoglundh, M.; and Grönbeck, H. First-principles microkinetic model for low-temperature NH3-assisted selective catalytic reduction of NO over Cu-CHA. *ACS Catal.*, *11* (2021), 14395–14407.

[57] Giordanino, F.; Borfecchia, E.; Lomachenko, K. A.; Lazzarini, A.; Agostini, G.; Gallo, E.; Soldatov, A. V.; Beato, P.; Bordiga, S.; and Lamberti, C. Interaction of NH3 with Cu-SSZ-13 catalyst: a complementary FTIR, XANES, and XES study. *J. Phys. Chem. letters*, *5* (2014), 1552–1559.

[58] Janssens, T. V.; Falsig, H.; Lundegaard, L. F.; Vennestrøm, P. N.; Rasmussen, S. B.; Moses, P. G.; Giordanino, F.; Borfecchia, E.; Lomachenko, K. A.; Lamberti, C.; et al. A consistent reaction scheme for the selective catalytic reduction of nitrogen oxides with ammonia. *ACS Catal.*, *5* (2015), 2832–2845.

[59] Lomachenko, K. A.; Borfecchia, E.; Negri, C.; Berlier, G.; Lamberti, C.; Beato, P.; Falsig, H.; and Bordiga, S. The Cu-CHA deNO x catalyst in action: temperature-dependent NH3-assisted selective catalytic reduction monitored by operando XAS and XES. *J. Am. Chem. Soc.*, *138* (2016), 12025–12028.

[60] Chen, L.; Jansson, J.; Skoglundh, M.; and Gronbeck, H. Mechanism for solid-state ion exchange of Cu+ into zeolites. *J. Phys. Chem. C*, *120* (2016), 29182–29189.

[61] Paolucci, C.; Khurana, I.; Parekh, A. A.; Li, S.; Shih, A. J.; Li, H.; Iorio, J. R. D.; Albarracin-caballero, J. D.; Yezerets, A.; Miller, J. T.; Delgass, W. N.; Ribeiro, F. H.; Schneider, W. F.; and Gounder, R. Dynamic Multinuclear Sites Formedby Mobilized Copper Ions in NOx Selective Catalytic Reduction. *Science*, *357* (2017), 898–903.

[62] Chen, L.; Falsig, H.; Janssens, T. V.; and Grönbeck, H. Activation of Oxygen on $(NH_3–Cu–NH_3)^+$ in NH_3-SCR over Cu-CHA. *J. Catal.*, *358* (2018), 179–186. ISSN 10902694. doi: 10.1016/j.jcat.2017.12.009.

[63] Janssens, T. V.; Borfecchia, E.; Lomachenko, K. A.; Grönbeck, H.; and Berlier, G. The [(NH3) 4Cu2O2] 2+-Peroxo Complex as the Key Intermediate for NH3-SCR Activity and Deactivation of Cu-CHA Catalysts. *ChemCatChem*, (2024), e202400384.

[64] Chen, L.; Janssens, T. V.; Vennestrøm, P. N.; Jansson, J.; Skoglundh, M.; and Grönbeck, H. A Complete Multisite Reaction Mechanism for Low-Temperature

NH_3-SCR over Cu-CHA. *ACS Catal.*, *10* (2020), 5646–5656. ISSN 21555435. doi: 10.1021/acscatal.0c00440.

[65] Singh, S. *Investigating hydrothermal stability and influence of water on the activity of Cu-CHA catalysts for NH3-SCR*. Chalmers Tekniska Hogskola (Sweden), 2024.

[66] Schrödinger, E. Quantisierung als eigenwertproblem. *Annalen der physik*, *385* (1926), 437–490.

[67] Born, M. and Oppenheimer, R. On the quantum theory of molecules. In *Quantum Chemistry: Classic Scientific Papers*, pages 1–24. World Scientific, 2000.

[68] Hartree, D. R. The wave mechanics of an atom with a non-Coulomb central field. Part I. Theory and methods. In *Mathematical Proceedings of the Cambridge Philosophical Society*, volume 24, pages 89–110. Cambridge university press, 1928.

[69] Fock, V. Näherungsmethode zur Lösung des quantenmechanischen Mehrkörperproblems. *Zeitschrift für Physik*, *61* (1930), 126–148.

[70] Martin, R. M. *Electronic structure: basic theory and practical methods*. Cambridge university press, 2020.

[71] Thomas, L. H. The calculation of atomic fields. In *Mathematical proceedings of the Cambridge philosophical society*, volume 23, pages 542–548. Cambridge University Press, 1927.

[72] Fermi, E. Statistical method to determine some properties of atoms. *Rend. Accad. Naz. Lincei*, *6* (1927), 5.

[73] Hohenberg, P. and Kohn, W. Inhomogeneous electron gas. *Phys. Rev.*, *136* (1964), B864.

[74] Hohenberg, P. and Kohn, W. Inhomogeneous Electron Gas. *Phys. Rev.*, *136* (1964), B864–B871.

[75] Kohn, W. and Sham, L. J. Self-consistent equations including exchange and correlation effects. *Phys. Rev.*, *140* (1965), A1133.

[76] Lee, J. G. *Computational materials science: an introduction*. CRC press, 2016.

[77] Sousa, S. F.; Fernandes, P. A.; and Ramos, M. J. General performance of density functionals. *J. Phys. Chem. A*, *111* (2007), 10439–10452.

[78] Ceperley, D. M. and Alder, B. J. Ground State of the Electron Gas by a Stochastic Method. *Phys. Rev. Lett.*, *45* (1980), 566–569.

[79] Perdew, J. P.; Burke, K.; and Ernzerhof, M. Generalized gradient approximation made simple. *Phys. Rev. Lett.*, *77* (1996), 3865.

[80] Perdew, J. P.; Chevary, J. A.; Vosko, S. H.; Jackson, K. A.; Pederson, M. R.; Singh, D. J.; and Fiolhais, C. Atoms, molecules, solids, and surfaces: Applications of the generalized gradient approximation for exchange and correlation. *Phys. Rev. B*, *46* (1992), 6671.

[81] Paier, J.; Hirschl, R.; Marsman, M.; and Kresse, G. The Perdew–Burke–Ernzerhof exchange-correlation functional applied to the G2-1 test set using a plane-wave basis set. *J. Chem. Phys.*, *122* (2005).

[82] Ernzerhof, M. and Scuseria, G. E. Assessment of the Perdew–Burke–Ernzerhof exchange-correlation functional. *J. Chem. Phys.*, *110* (1999), 5029–5036.

[83] Kurth, S.; Perdew, J. P.; and Blaha, P. Molecular and solid-state tests of density functional approximations: LSD, GGAs, and meta-GGAs. *Int. J. Quantum Chem.*, *75* (1999), 889–909.

[84] Sholl, D. S. and Steckel, J. A. *Density functional theory: a practical introduction*. John Wiley & Sons, 2022.

[85] Anisimov, V. I.; Zaanen, J.; and Andersen, O. K. Band theory and Mott insulators: Hubbard U instead of Stoner I. *Phys. Rev. B*, *44* (1991), 943.

[86] Himmetoglu, B.; Floris, A.; De Gironcoli, S.; and Cococcioni, M. Hubbard-corrected DFT energy functionals: The LDA+ U description of correlated systems. *Int. J. Quantum Chem.*, *114* (2014), 14–49.

[87] Grimme, S.; Antony, J.; Ehrlich, S.; and Krieg, H. A consistent and accurate ab initio parametrization of density functional dispersion correction (DFT-D) for the 94 elements H-Pu. *J. Chem. Phys.*, *132* (2010).

[88] Grimme, S. Semiempirical GGA-type density functional constructed with a long-range dispersion correction. *J. Comput. Chem.*, *27* (2006), 1787–1799.

[89] Kresse, G. and Furthmüller, J. Efficient iterative schemes for ab initio total-energy calculations using a plane-wave basis set. *Phys. Rev. B*, *54* (1996), 11169.

[90] Blöchl, P. E. Projector augmented-wave method. *Phys. Rev. B*, *50* (1994), 17953.

[91] Heine, V. The pseudopotential concept. *Solid state physics*, *24* (1970), 1–36.

[92] Hellman, H. Einführung in die Quantenchemie. *Franz Deuticke, Leipzig*, *285* (1937), 90.

[93] Feynman, R. P. Forces in molecules. *Phys. Rev.*, *56* (1939), 340.

[94] Xi, Y.; Su, C.; Ottinger, N. A.; and Liu, Z. G. Effects of hydrothermal aging on the sulfur poisoning of a Cu-SSZ-13 SCR catalyst. *Appl. Catal. B: Environ.*, *284* (2021), 119749.

[95] Arrhenius, S. Üon the reaction rate during the inversion of cane sugar by acids. *J. Phys. Chem.*, *4* (1889), 226–248.

[96] Logan, S. The origin and status of the Arrhenius equation. *Journal of Chemical Education*, *59* (1982), 279.

[97] Sheppard, D.; Terrell, R.; and Henkelman, G. Optimization methods for finding minimum energy paths. *J. Chem. Phys.*, *128* (2008).

[98] Henkelman, G.; Uberuaga, B. P.; and Jónsson, H. A climbing image nudged elastic band method for finding saddle points and minimum energy paths. *J. Chem. Phys.*, *113* (2000), 9901–9904.

[99] Henkelman, G. and Jónsson, H. Improved tangent estimate in the nudged elastic band method for finding minimum energy paths and saddle points. *J. Chem. Phys.*, *113* (2000), 9978–9985.

[100] Baker, J. Molecular structure and vibrational spectra. *Handbook of Computational Chemistry*, (2012), 423–496.

[101] Barnett, R.; Landman, U.; Nitzan, A.; and Rajagopal, G. Born–Oppenheimer dynamics using density-functional theory: Equilibrium and fragmentation of small sodium clusters. *J. Chem. Phys.*, *94* (1991), 608–616.

[102] Car, R. and Parrinello, M. Unified approach for molecular dynamics and density-functional theory. *Phys. Rev. Lett.*, *55* (1985), 2471.

[103] Nosé, S. A unified formulation of the constant temperature molecular dynamics methods. *J. Chem. Phys.*, *81* (1984), 511–519.

[104] Nosé, S. A molecular dynamics method for simulations in the canonical ensemble. *Molecular physics*, *52* (1984), 255–268.

[105] Hoover, W. G. Canonical dynamics: Equilibrium phase-space distributions. *Phys. Rev. A*, *31* (1985), 1695.

[106] Filot, I. *Introduction to microkinetic modeling*. Technische Universiteit Eindhoven, December 2018. ISBN 978-90-386-4520-9.

[107] Eyring, H. The activated complex and the absolute rate of chemical reactions. *Chem. Rev.*, *17* (1935), 65–77.

[108] Motagamwala, A. H. and Dumesic, J. A. Microkinetic modeling: a tool for rational catalyst design. *Chem. Rev.*, *121* (2020), 1049–1076.

[109] Bonhomme, C.; Gervais, C.; Babonneau, F.; Coelho, C.; Pourpoint, F.; Azais, T.; Ashbrook, S. E.; Griffin, J. M.; Yates, J. R.; Mauri, F.; et al. First-principles calculation of NMR parameters using the gauge including projector augmented wave method: a chemist's point of view. *Chem. Rev.*, *112* (2012), 5733–5779.

[110] Pickard, C. J. and Mauri, F. All-electron magnetic response with pseudopotentials: NMR chemical shifts. *Phys. Rev. B*, *63* (2001), 245101.

[111] Petrilli, H. M.; Blöchl, P. E.; Blaha, P.; and Schwarz, K. Electric-field-gradient calculations using the projector augmented wave method. *Phys. Rev. B*, *57* (1998), 14690.

[112] Vanlommel, S.; Hoffman, A. E.; Smet, S.; Radhakrishnan, S.; Asselman, K.; Chandran, C. V.; Breynaert, E.; Kirschhock, C. E.; Martens, J. A.; and Van Speybroeck, V. How Water and Ion Mobility Affect the NMR Fingerprints of the Hydrated JBW Zeolite: A Combined Computational-Experimental Investigation. *Chem. Eur. J.*, *28* (2022), e202202621.

[113] Nellessen, A. Modified Vanadium Oxide Catalysts for the Selective Catalytic Reduction of NOx. (2025).

[114] Niwa, M. and Katada, N. New method for the temperature-programmed desorption (TPD) of ammonia experiment for characterization of zeolite acidity: a review. *Chem. Rec.*, *13* (2013), 432–455.

[115] Schroeder, S. L. and Gottfried, M. Temperature-programmed desorption (TPD) thermal desorption spectroscopy (TDS). *Adv. Phys. Chem. Lab, FU Berlin*, (2002), 1–22.

[116] Molokova, A. Y.; Salusso, D.; Borfecchia, E.; Wen, F.; Magliocco, S.; Bordiga, S.; Janssens, T. V.; Lomachenko, K. A.; and Berlier, G. The chemical nature of SO 2 poisoning of Cu-CHA-based SCR catalysts for NOx removal in diesel exhausts. *Catal. Sci. Technol.*, *14* (2024), 5989–5995.

[117] Negri, C.; Selleri, T.; Borfecchia, E.; Martini, A.; Lomachenko, K. A.; Janssens, T. V.; Cutini, M.; Bordiga, S.; and Berlier, G. Structure and reactivity of oxygen-bridged diamino dicopper (II) complexes in Cu-ion-exchanged chabazite catalyst for NH3-mediated selective catalytic reduction. *J. Am. Chem. Soc.*, *142* (2020), 15884–15896.

[118] Molokova, A. Y.; Borfecchia, E.; Martini, A.; Pankin, I. A.; Atzori, C.; Mathon, O.; Bordiga, S.; Wen, F.; Vennestrøm, P. N.; Berlier, G.; et al. SO2 Poisoning of Cu-CHA deNO x Catalyst: The Most Vulnerable Cu Species Identified by X-ray Absorption Spectroscopy. *JACS Au*, *2* (2022), 787–792.

[119] Nasello, N. D.; Usberti, N.; Iacobone, U.; Gramigni, F.; Hu, W.; Liu, S.; Nova, I.; Gao, X.; and Tronconi, E. Dual-Site RHC and OHC transient kinetics predict low-T standard SCR steady-state rates over a Cu-CHA catalyst. *ACS Catal.*, *13* (2023), 2723–2734.

[120] Partridge, W. P.; Joshi, S. Y.; Pihl, J. A.; and Currier, N. W. New operando method for quantifying the relative half-cycle rates of the NO SCR redox cycle over Cu-exchanged zeolites. *Appl. Catal. B: Environ.*, *236* (2018), 195–204.

[121] Gao, F.; Walter, E. D.; Karp, E. M.; Luo, J.; Tonkyn, R. G.; Kwak, J. H.; Szanyi, J.; and Peden, C. H. Structure–activity relationships in NH3-SCR over Cu-SSZ-13 as probed by reaction kinetics and EPR studies. *J. Catal.*, *300* (2013), 20–29.

[122] Feng, Y.; Janssens, T. V.; Vennestrøm, P. N.; Jansson, J.; Skoglundh, M.; and Gronbeck, H. The role of H+-and Cu+-sites for N2O formation during NH3-SCR over Cu-CHA. *J. Phys. Chem. C*, *125* (2021), 4595–4601.

[123] Sano, T.; Ikeya, H.; Kasuno, T.; Wang, Z.; Kawakami, Y.; and Soga, K. Influence of crystallinity of HZSM-5 zeolite on its dealumination rate. *Zeolites*, *19* (1997), 80–86.

[124] Luo, J.; Gao, F.; Kamasamudram, K.; Currier, N.; Peden, C. H.; and Yezerets, A. New insights into Cu/SSZ-13 SCR catalyst acidity. Part I: Nature of acidic sites probed by NH3 titration. *J. Catal.*, *348* (2017), 291–299.

[125] Schmidt, J. E.; Oord, R.; Guo, W.; Poplawsky, J. D.; and Weckhuysen, B. M. Nanoscale tomography reveals the deactivation of automotive copper-exchanged zeolite catalysts. *Nat. Commun.*, *8* (2017), 1666.

[126] Vennestrøm, P. N.; Janssens, T. V.; Kustov, A.; Grill, M.; Puig-Molina, A.; Lundegaard, L. F.; Tiruvalam, R. R.; Concepción, P.; and Corma, A. Influence of lattice stability on hydrothermal deactivation of Cu-ZSM-5 and Cu-IM-5 zeolites for selective catalytic reduction of NOx by NH3. *J. Catal.*, *309* (2014), 477–490.

[127] Song, J.; Wang, Y.; Walter, E. D.; Washton, N. M.; Mei, D.; Kovarik, L.; Engelhard, M. H.; Prodinger, S.; Wang, Y.; Peden, C. H.; et al. Toward rational design of Cu/SSZ-13 selective catalytic reduction catalysts: implications from atomic-level understanding of hydrothermal stability. *ACS Catal.*, *7* (2017), 8214–8227.

[128] Fickel, D. W.; D'Addio, E.; Lauterbach, J. A.; and Lobo, R. F. The ammonia selective catalytic reduction activity of copper-exchanged small-pore zeolites. *Appl. Catal. B: Environ.*, *102* (2011), 441–448.

[129] Han, S.; Cheng, J.; Zheng, C.; Ye, Q.; Cheng, S.; Kang, T.; and Dai, H. Effect of Si/Al ratio on catalytic performance of hydrothermally aged Cu-SSZ-13 for the NH3-SCR of NO in simulated diesel exhaust. *Appl. Surf. Sci.*, *419* (2017), 382–392.

[130] Brookshear, D. W.; Nam, J.-g.; Nguyen, K.; Toops, T. J.; and Binder, A. Impact of sulfation and desulfation on NOx reduction using Cu-chabazite SCR catalysts. *Catal. Today*, *258* (2015), 359–366.

[131] Hammershøi, P. S.; Jensen, A. D.; and Janssens, T. V. Impact of SO2-poisoning over the lifetime of a Cu-CHA catalyst for NH3-SCR. *Appl. Catal. B: Environ.*, *238* (2018), 104–110.

[132] Bjerregaard, J. D.; Votsmeier, M.; and Groenbeck, H. Mechanism for SO2 poisoning of Cu-CHA during low temperature NH3-SCR. *J. Catal.*, *417* (2023), 497–506.

[133] Molokova, A. Y.; Abasabadi, R. K.; Borfecchia, E.; Mathon, O.; Bordiga, S.; Wen, F.; Berlier, G.; Janssens, T. V.; and Lomachenko, K. A. Elucidating the reaction mechanism of SO 2 with Cu-CHA catalysts for NH 3-SCR by X-ray absorption spectroscopy. *Chem. Sci.*, *14* (2023), 11521–11531.

[134] Wijayanti, K.; Xie, K.; Kumar, A.; Kamasamudram, K.; and Olsson, L. Effect of gas compositions on SO2 poisoning over Cu/SSZ-13 used for NH3-SCR. *Appl. Catal. B: Environ.*, *219* (2017), 142–154.

[135] Mesilov, V.; Dahlin, S.; Bergman, S. L.; Hammershøi, P. S.; Xi, S.; Pettersson, L. J.; and Bernasek, S. L. Insights into sulfur poisoning and regeneration of Cu-SSZ-13 catalysts: in situ Cu and S K-edge XAS studies. *Catal. Sci. Technol.*, *11* (2021), 5619–5632.

[136] Fickel, D. W. and Lobo, R. F. Copper coordination in Cu-SSZ-13 and Cu-SSZ-16 investigated by variable-temperature XRD. *J. Phys. Chem. C*, *114* (2010), 1633–1640.